REPORT DOCUMENTATION PAGE

Form Approved OMB NO. 0704-0188

The public reporting burden for this collection of information is estimated to average 1 hour per response, including the time for reviewing instructions, searching existing data sources, gathering and maintaining the data needed, and completing and reviewing the collection of information. Send comments regarding this burden estimate or any other aspect of this collection of information, including suggesstions for reducing this burden, to Washington Headquarters Services, Directorate for Information Operations and Reports, 1215 Jefferson Davis Highway, Suite 1204, Arlington VA, 22202-4302. Respondents should be aware that notwithstanding any other provision of law, no person shall be subject to any oenalty for failing to comply with a collection of information if it does not display a currently valid OMB control number.
PLEASE DO NOT RETURN YOUR FORM TO THE ABOVE ADDRESS.

1. REPORT DATE (DD-MM-YYYY)	2. REPORT TYPE	3. DATES COVERED (From - To)
16-11-2016	Final Report	1-Jun-2012 - 31-May-2016

4. TITLE AND SUBTITLE
Final Report: Mechanical and Ferroelectric Response of Highly Textured PZT Films for Low Power MEMS

5a. CONTRACT NUMBER
W911NF-12-1-0204

5b. GRANT NUMBER

5c. PROGRAM ELEMENT NUMBER
611102

6. AUTHORS
Ioannis Chasiotis (PI), Debashish Das (graduate student)

5d. PROJECT NUMBER

5e. TASK NUMBER

5f. WORK UNIT NUMBER

7. PERFORMING ORGANIZATION NAMES AND ADDRESSES
University of Illinois - Urbana - Champaign
c/o Office of Sponsored Programs
1901 S. First Street, Suite A
Champaign, IL 61820 -7406

8. PERFORMING ORGANIZATION REPORT NUMBER

9. SPONSORING/MONITORING AGENCY NAME(S) AND ADDRESS (ES)
U.S. Army Research Office
P.O. Box 12211
Research Triangle Park, NC 27709-2211

10. SPONSOR/MONITOR'S ACRONYM(S)
ARO

11. SPONSOR/MONITOR'S REPORT NUMBER(S)
62202-EG.5

12. DISTRIBUTION AVAILIBILITY STATEMENT
Approved for Public Release; Distribution Unlimited

13. SUPPLEMENTARY NOTES
The views, opinions and/or findings contained in this report are those of the author(s) and should not contrued as an official Department of the Army position, policy or decision, unless so designated by other documentation.

14. ABSTRACT
This program investigated the elastic and inelastic behavior of textured Pt and PZT thin films integrated in PZT-based MEMS. The effect of film thickness and grain size on the mechanical response of freestanding nanocrystalline {111}-textured Pt films, with thicknesses in the range of 100 to 1000 nm, was experimentally and analytically investigated. The measured elastic modulus of Pt (167±2 GPa) agreed well with theoretical estimates for {111}-textured polycrystalline Pt. The experimentally determined proportional limit was consistent with predictions by a modified Thompson model for plastic deformation of polycrystalline columnar metal films, while a

15. SUBJECT TERMS
Pt, PZT, Thin films, MEMS, mechanical properties, ferroelectric properties, film texture, strain rate

16. SECURITY CLASSIFICATION OF:			17. LIMITATION OF ABSTRACT	15. NUMBER OF PAGES	19a. NAME OF RESPONSIBLE PERSON
a. REPORT	b. ABSTRACT	c. THIS PAGE			Ioannis Chasiotis
UU	UU	UU	UU		19b. TELEPHONE NUMBER 217-244-1474

Standard Form 298 (Rev 8/98)
Prescribed by ANSI Std. Z39.18

Report Title

Final Report: Mechanical and Ferroelectric Response of Highly Textured PZT Films for Low Power MEMS

ABSTRACT

This program investigated the elastic and inelastic behavior of textured Pt and PZT thin films integrated in PZT-based MEMS. The effect of film thickness and grain size on the mechanical response of freestanding nanocrystalline {111}-textured Pt films, with thicknesses in the range of 100 to 1000 nm, was experimentally and analytically investigated. The measured elastic modulus of Pt (167±2 GPa) agreed well with theoretical estimates for {111}-textured polycrystalline Pt. The experimentally determined proportional limit was consistent with predictions by a modified Thompson model for plastic deformation of polycrystalline columnar metal films, while a Taylor strain hardening model was superimposed to the modified Thompson model to account for additional hardening due to dislocation interactions. The effect of texture on the open-circuit mechanical response and piezoelectric properties of 500-nm thick freestanding PZT films was also investigated. The open circuit modulus varied linearly between 90±2 GPa for (001) texture and 122±3 GPa for (111) texture. (001) texture resulted in the most pronounced non-linear stress-strain response indicating easier 90? domain switching. The piezoelectric properties depended strongly on the PZT film texture: PZT films with high %(001) texture content demonstrated much more pronounced piezoelectric response than those with high %(111) texture content.

Enter List of papers submitted or published that acknowledge ARO support from the start of the project to the date of this printing. List the papers, including journal references, in the following categories:

(a) Papers published in peer-reviewed journals (N/A for none)

Received	Paper

TOTAL:

Number of Papers published in peer-reviewed journals:

(b) Papers published in non-peer-reviewed journals (N/A for none)

Received	Paper

TOTAL:

Number of Papers published in non peer-reviewed journals:

(c) Presentations

Debashish Das, Luz Sanchez, Joel Martin, Brian Power, Steven Isaacson,
Ronald Polcawich, and Ioannis Chasiotis, “Mechanical, Ferroelastic and Piezoelectric Behavior of Highly Textured PZT Films” Poster Presentation, TMS 2016, The Minerals, Metals and Materials Society, February 14-18, 2016, Nashville, TN, USA.

Number of Presentations: 1.00

Non Peer-Reviewed Conference Proceeding publications (other than abstracts):

Received	Paper

TOTAL:

Number of Non Peer-Reviewed Conference Proceeding publications (other than abstracts):

Peer-Reviewed Conference Proceeding publications (other than abstracts):

Received	Paper

TOTAL:

Number of Peer-Reviewed Conference Proceeding publications (other than abstracts):

(d) Manuscripts

Received	Paper	
08/27/2015	2.00	Dedashish Das, B. Power, J. Martin, Ron G. Polcawich, I. Chasiotis. Role of Seeding Layer in the Inelastic Response of Submicron and Nanometer Thick {111}-textured Pt Films, Materials Science and Engineering A (09 2015)

TOTAL: **1**

Number of Manuscripts:

Books

Received Book

TOTAL:

Received Book Chapter

TOTAL:

Patents Submitted

Patents Awarded

Awards

• 2016: PI Chasiotis was elected a University of Illinois Scholar. In total, six faculty of the entire campus of the University of Illinois at Urbana-Champaign (with ~1,800 tenured and tenure-track faculty) were elected University Scholars in 2016.

• 2016: PI Chasiotis was elected as the Editor-in-Chief of the journal Experimental Mechanics, the flagship journal of the Society for Experimental Mechanics (SEM). The journal has 56 year history. This is a 5-year appointment.

• 2015: PI Chasiotis was elected a Fellow of the American Society for Mechanical Engineers (ASME).

• 2013: PI Chasiotis received A.J. Durelli Award by the Society for Experimental Mechanics. The award recognizes a young professional who has introduced, or helped to introduce, an innovative approach and/or method into the field of experimental mechanics.

• 2012: PI Chasiotis and his ARL collaborators received the Hetenyi Best Paper Award for their paper in Experimental Mechanics. The work presented in that paper was based on collaborative research with the ARL, which was sponsored by the ARO.

Graduate Students

NAME	PERCENT_SUPPORTED	Discipline
Debashish Das	0.50	
FTE Equivalent:	**0.50**	
Total Number:	**1**	

Names of Post Doctorates

NAME	PERCENT_SUPPORTED
FTE Equivalent:	
Total Number:	

Names of Faculty Supported

NAME	PERCENT_SUPPORTED	National Academy Member
Ioannis Chasiotis	0.04	
FTE Equivalent:	**0.04**	
Total Number:	**1**	

Names of Under Graduate students supported

NAME	PERCENT_SUPPORTED
FTE Equivalent:	
Total Number:	

Student Metrics

This section only applies to graduating undergraduates supported by this agreement in this reporting period

The number of undergraduates funded by this agreement who graduated during this period: 0.00

The number of undergraduates funded by this agreement who graduated during this period with a degree in science, mathematics, engineering, or technology fields:..... 0.00

The number of undergraduates funded by your agreement who graduated during this period and will continue to pursue a graduate or Ph.D. degree in science, mathematics, engineering, or technology fields:..... 0.00

Number of graduating undergraduates who achieved a 3.5 GPA to 4.0 (4.0 max scale):..... 0.00

Number of graduating undergraduates funded by a DoD funded Center of Excellence grant for Education, Research and Engineering:..... 0.00

The number of undergraduates funded by your agreement who graduated during this period and intend to work for the Department of Defense 0.00

The number of undergraduates funded by your agreement who graduated during this period and will receive scholarships or fellowships for further studies in science, mathematics, engineering or technology fields: 0.00

Names of Personnel receiving masters degrees

NAME
Total Number:

Names of personnel receiving PHDs

NAME

Total Number:

Names of other research staff

NAME PERCENT_SUPPORTED

FTE Equivalent:
Total Number:

Sub Contractors (DD882)

Inventions (DD882)

Scientific Progress

1. Role of Oxide Seed Layer in Plastic Response of Expitaxially Grown Polycrystalline Pt Films:

• The effect of film thickness and grain size on the mechanical response of freestanding nanocrystalline {111}-textured Pt films that were epitaxially grown on rutile TiO2 seed substrates with columnar grain structure was experimentally and analytically investigated for Pt/TiO2 bilayer films with thicknesses in the range of 50-1000 nm.
• The measured elastic modulus of Pt (167±2 GPa) agreed well with theoretical calculations of the in-plane modulus of {111}-textured polycrystalline Pt, while the modulus of TiO2 (195±5 GPa) was 15% lower than the theoretical estimate for (100)-textured polycrystalline TiO2. The flow stress of Pt/TiO2 films increased with reduced film thickness. The experimentally determined proportional limit of Pt was consistent with predictions by a modified Thompson model for plastic deformation of polycrystalline columnar metal films. A Taylor strain hardening model was superimposed to the modified Thompson model to account for additional hardening occurring as a result of dislocation interactions during plastic deformation of the Pt films.
• Knowledge of the mechanical response of the Pt films was integral to this project, as the properties of Pt are used to extract the properties of the PZT layer in SiO2-TiO2-Pt-PZT laminates.

2. Control of Mechanical and Ferroelectric Properties of Textured PZT Films:

• The effect of texture on the open-circuit mechanical response and piezoelectric properties of 500-nm thick freestanding PZT films was investigated.
• Pure (001) texture resulted in the most pronounced non-linear stress-strain response and (111) texture in the least non-linear response, indicating more pronounced 90? domain switching for pure (001) texture, which was also corroborated by a micromechanics model. This implies that the non-linear mechanical behavior due to ferroelasticity could be controlled through film texture with a preference to (111) texture.
• The open circuit modulus was found to vary linearly with %(001) and %(111) texture factors ranging between 90±2 GPa for pure (001) texture and 122±3 GPa for pure (111) texture.
• The piezoelectric properties were found to depend on film texture: the transverse strain and stress coefficients varied linearly with %(001) and %(111) texture factors, and increased with increasing %(001) texture.
• Films with higher percentage of (001) texture demonstrated stronger piezoelectric response than those with higher (111) texture content.

[SEE ALSO ATTACHMENT]

Technology Transfer

• The results of this research were shared on a regular basis with Dr. R. Polcawich at the Specialty Electronic Materials and Sensor Cleanroom and Lab of the ARL in Adelphi, MD, who provided us with test specimens.

• The PI visited this ARL facility several times in the past. His student who worked on this project (D. Das) visited the ARL facility in Adelphi, MD in August 2015 to conduct research and obtain electrical and displacement measurements on PZT unimorphs.

• We published 2 joint journal papers with the collaborators at ARL. A third joint journal paper will be submitted by the end of 2016.

Final Project Report: Grant # W911NF-12-1-0204

(June 2012 – August 2016)

Effort Title: Mechanical and Ferroelectric Response of Highly Textured PZT Films for Low Power MEMS

PI: Prof. Ioannis Chasiotis

Aerospace Engineering, University of Illinois at Urbana-Champaign, IL, 61801

I. PROJECT SUMMARY

I.A. Objectives

The objective of this research program was to investigate the electromechanical response of Lead Zirconate Titanate, $Pb(Zr_{0.52}Ti_{0.48})O_3$ (PZT) thin films that are fabricated for Microelectromechanical Systems (MEMS), as a function of texture that ranges from strong (111) to strong (001) texture. Substantial improvements in MEMS performance can be achieved with proper selection of the optimum texture leading to the highest piezoelectric coefficients, such as lower actuation voltage, increased actuation force and decreased power consumption. In this work, texture-electromechanical property relationships for freestanding PZT film stacks with total thickness of 1 μm were obtained for the first time, which are relevant to advanced MEMS applications.

I.B. Approach

The effect of texture on the electromechanical response of PZT-based thin film stacks was quantified experimentally and analytical models were applied or developed to simulate the experimental results. Laminates with the general sequence of PZT/Pt/SiO_2 are employed in MEMS applications hence the properties of all auxiliary layers are needed in order to obtain the mechanical response of the PZT layer alone. As a result, experiments were carried out with individual SiO_2 films and combinations of TiO_2-Pt, SiO_2-TiO_2-Pt, SiO_2-TiO_2-Pt-PZT and SiO_2-TiO_2-Pt-PZT-Pt-ALD to determine the mechanical behavior of each layer. The experimental data were then used to extract the fundamental mechanical and ferroelectric properties of textured PZT films, and thus provide fabrication-structure-property relationships for the design of improved PZT MEMS. Specifically, we:

- Quantified the mechanical response of highly {111}-textured Pt thin films with thicknesses ranging between 50-1000 nm on 35-50 nm thick {100}-textured TiO_2, as a function of Pt

film thickness and grain size via microscale uniaxial tension experiments on patterned dog-bone and microscale thin film specimens. Additionally, mechanistic models were developed to explain the variation of flow stress with microstructural grain size, film thickness and plastic strain.

- Quantified the open circuit elastic modulus and mechanical strength of textured PZT film stacks as a function of texture using our group's experimental method for full-field strain measurements at the submicron scale with the aid of Digital Image Correlation (DIC). Microscale uniaxial tension experiments were carried out with SiO_2, TiO_2-Pt, SiO_2-TiO_2-Pt, SiO_2-TiO_2-Pt-PZT and SiO_2-TiO_2-Pt-PZT-Pt-ALD stacks that were patterned into microscale thin-film dog-bone shaped specimens. A micromechanics model was developed to explain the observed non-linearity in the stress-strain response of 100% (001) and 100% (111) textured PZT films.
- Evaluated the piezoelectric coefficients as a function of PZT texture by using Laser Doppler Vibrometer (LDV) measurements of the out-of-plane bending of unimorphs subjected to a unipolar bias. An analytical model was modified and used to relate the out-of-plane displacements of multilayered bending actuators to the transverse piezoelectric strain coefficients, $d_{31,f}$ which were then converted into piezoelectric stress coefficients, $e_{31,f}$. Additionally, the out-of-plane deflection of textured PZT unimorphs was measured via bipolar bias when polarization reversals took place.
- Electrical, polarization vs. electric field (PE), and capacitance vs. voltage (CV) measurements were carried out on textured PZT unimorphs. Furthermore, the resonant frequencies were measured for different textured freestanding PZT films.

I.B.1. Uniqueness of Approach

In recent years the use of TiO_2 as an adhesion layer, highly {111} textured Pt electrodes, and a $PbTiO_3$ seed layer with varying Pb-excess content have enabled the control of texture in thin PZT films. (001) PZT is particularly preferred because of its high piezoelectric coefficients that could increase the actuation force by as much as 30-50%. Prior work by the PI's group with non-textured PZT films served as important reference for the results obtained in this program, because **(a)** existing data could be used for comparison, and **(b)** the same proven experimental methods were applied to eliminate any measurement uncertainties.

Previous studies on the mechanical behavior of PZT films using nanoindentation and membrane deflection techniques were limited to films bonded on substrates, small deflections and stresses, large specimen sizes, and mostly non-textured films. Furthermore, nanoindentation

experiments cannot obtain the failure strain and do not facilitate an accurate extraction of the elastic modulus due to the inherent non-linear behavior of PZT thin films. More importantly, the much needed in-plane mechanical properties cannot be obtained by point contact methods. The microscale tension tests conducted in this study on freestanding PZT stacks overcame the aforementioned difficulties.

I.C. Major Accomplishments

I.C.1. Role of Oxide Seed Layer in Plastic Response of Expitaxially Grown Polycrystalline Pt Films

- The effect of film thickness and grain size on the mechanical response of freestanding nanocrystalline {111}-textured Pt films that were epitaxially grown on rutile TiO_2 seed substrates with columnar grain structure was experimentally and analytically investigated for Pt/TiO_2 bilayer films with thicknesses in the range of 50-1000 nm.
- The measured elastic modulus of Pt (167±2 GPa) agreed well with theoretical calculations of the in-plane modulus of {111}-textured polycrystalline Pt, while the modulus of TiO_2 (195±5 GPa) was 15% lower than the theoretical estimate for (100)-textured polycrystalline TiO_2. The flow stress of Pt/TiO_2 films increased with reduced film thickness. The experimentally determined proportional limit of Pt was consistent with predictions by a modified Thompson model for plastic deformation of polycrystalline columnar metal films. A Taylor strain hardening model was superimposed to the modified Thompson model to account for additional hardening occurring as a result of dislocation interactions during plastic deformation of the Pt films.
- Knowledge of the mechanical response of the Pt films was integral to this project, as the properties of Pt are used to extract the properties of the PZT layer in SiO_2-TiO_2-Pt-PZT laminates.

I.C.2. Control of Mechanical and Ferroelectric Properties of Textured PZT Films

- The effect of texture on the open-circuit mechanical response and piezoelectric properties of 500-nm thick freestanding PZT films was investigated.
- Pure (001) texture resulted in the most pronounced non-linear stress-strain response and (111) texture in the least non-linear response, indicating more pronounced 90˚ domain switching for pure (001) texture, which was also corroborated by a micromechanics model.

This implies that the non-linear mechanical behavior due to ferroelasticity could be controlled through film texture with a preference to (111) texture.

- The open circuit modulus was found to vary linearly with %(001) and %(111) texture factors ranging between 90±2 GPa for pure (001) texture and 122±3 GPa for pure (111) texture.
- The piezoelectric properties were found to depend on film texture: the transverse strain and stress coefficients varied linearly with %(001) and %(111) texture factors, and increased with increasing %(001) texture.
- Films with higher percentage of (001) texture demonstrated stronger piezoelectric response than those with higher (111) texture content.

I.D. Relevance to the Army Mission

The research conducted in this program generated quantitative feedback to PZT-MEMS manufacturing, which, in turn, has the potential to accelerate the deployment of advanced PZT MEMS sensors or actuators in Army and civilian applications. PZT MEMS could revolutionize microscale actuators and sensors by enabling low-power microdevices as an alternative to existing electrostatic MEMS which have been limited by large bias voltage requirements. The ARL group in Adelphi, MD (collaborator in this project) has demonstrated highly efficient piezoelectric millimeter-scale robots, mechanical logic chips, radio-frequency (RF) components, power harvesters, etc. During the course of this program, we interacted on a regular basis with researchers at the ARL, and our results were frequently transitioned to them in the form of measurements of fundamental properties of PZT films.

I.E. Collaborations and Technology Transfer

- The results of this research were shared on a regular basis with Dr. R. Polcawich at the Specialty Electronic Materials and Sensor Cleanroom and Lab of the ARL in Adelphi, MD, who provided us with test specimens.
- The PI visited this ARL facility several times in the past. His student who worked on this project (D. Das) visited the ARL facility in Adelphi, MD in August 2015 to conduct research and obtain electrical and displacement measurements on PZT unimorphs.
- We published 2 joint journal papers with the particular ARL group (see below). A third joint journal paper will be submitted by the end of 2016.

II.A. Resulting Journal Publications

JOURNAL PUBLICATIONS

- D. Das, B. Power, J. Martin, R.G. Polcawich, I. Chasiotis, "Role of Oxide Seed Layer in Plastic Response of Epitaxially Grown Textured Metal Films." *Acta Materialia* **112**, pp. 390-402, (2016).
- D. Das, L. Sanchez, J. Martin, B. Power, S. Isaacson, R.G. Polcawich, I. Chasiotis, "Control of the Mechanical Response of PbZr0.52Ti0.48O3 (PZT) Films through Texture." *Applied Physics Letters* **109**, pp. 131905, (2016).
- D. Das, L. Sanchez, J. Martin, B. Power, S. Isaacson, R.G. Polcawich, I. Chasiotis. Control of Ferroelectric Properties of $PbZr_{0.52}Ti_{0.48}O_3$ (PZT) Films through Texture. To be submitted to *Sensors and Actuators A:Physical* (2016).

SEMINARS AND CONFERENCES PRESENTED

- "Mechanical and Ferroelectric Behavior of PZT-based Thin Films for MEMS", Poster Presentation at PiezoMEMS 2013, April 9-10, 2013, Washington DC.
- "Mechanical Property Size Effects in Submicron and Nanometer Thick Textured Pt Films", Technical Presentation, ASME IMECE 2014, November 14-20, 2014, Montreal, Canada.
- "Size Effects in Mechanical Behavior of Submicron and Nanometer Thick Textured Pt Films", Technical Presentation given at SES 2014, October 1-3, 2014, Purdue, Indiana.
- "Mechanical, Ferroelastic and Piezoelectric Behavior of Highly Textured PZT Films" Poster Presentation, TMS 2016, The Minerals, Metals and Materials Society, February 14-18, 2016, Nashville, TN, USA.

II.B. Graduate Students Involved in this Project

- Debashish Das (Ph.D. student; Graduation in December 2016)

II.C. Awards, Honors and Appointments

- In 2016, the PI Chasiotis was elected a University of Illinois Scholar. In total, six faculty of the entire campus of the University of Illinois at Urbana-Champaign (with ~1,800 tenured and tenure-track faculty) were elected University Scholars in 2016.
- In 2016, the PI Chasiotis was elected as the Editor-in-Chief of the journal *Experimental Mechanics*, the flagship journal of the Society for Experimental Mechanics (SEM). The journal has 56 year history. This is a 5-year appointment.
- In 2015, the PI Chasiotis was elected a Fellow of the American Society for Mechanical Engineers (ASME).
- In 2013, the PI Chasiotis received A.J. Durelli Award by the *Society for Experimental Mechanics*. The award recognizes a young professional who has introduced, or helped to introduce, an innovative approach and/or method into the field of experimental mechanics.
- In 2012, the PI Chasiotis and his ARL collaborators received the Hetenyi Best Paper Award for their paper in *Experimental Mechanics*. The work presented in that paper was based on collaborative research with the ARL, which was sponsored by the ARO.

II.D. Acknowledgements

The PI acknowledges the support by ARO Grant # W911NF-12-1-0204 with Drs. Larry Russell and Asher Rubinstein as the program managers. The PI and his graduate student are grateful of the support and invaluable discussions with Dr. Ronald Polcawich and his collaborators at the Army Research Laboratory in Adelphi MD. Finally, FIB, SEM and X-Ray studies were carried out at the Frederick Seitz Materials Research Laboratory Central Research Facilities, University of Illinois.

III. DETAILED RESEARCH REPORT

III.A. Role of Oxide Seed Layer in Plastic Response of Expitaxial Polycrystalline Pt Films

Metallic thin films in freestanding form or deposited on substrates have been shown to exceed the flow stress of their bulk counterparts: Experiments with face-centered cubic (FCC) Ag, Al, Au, Cu, Ni, Pb films with thicknesses of 50 - 2,000 μm have shown that the flow stress increases with decreasing film thickness [1-9]. In the case of metal films deposited on substrates, mechanistic models have been developed to explain this inverse film thickness dependence of flow stress. Based on the threading dislocation concept by Freund for a film bonded to a substrate with some mismatch strain [10], Nix [11] developed a quantitative model considering the film/oxide and film/substrate interfaces acting as impenetrable obstacles to dislocation motion, thus necessitating the deposition of misfit dislocations at interfaces. Later, Thompson [12] extended the Nix-Freund model to polycrystalline films with grain diameters that are at least twice as large as the film thickness by including grain boundaries (GBs) as additional obstacles to dislocation motion. The two models combined could qualitatively explain the inverse film thickness and grain size dependence of flow stress that was experimentally observed for Al films deposited on Si substrates with an anodic oxide layer at the top surface [2]. Both the Nix-Freund and the Thompson models showed that the film texture influenced the yield stress.

In-situ TEM studies of thermally strained, epitaxially grown, single crystal Al [13] and Cu films [7] on (0001) α-Al_2O_3 substrates revealed the motion of threading dislocations on inclined {111} planes with the eventual deposition of interfacial dislocation segments at Al/α-Al_2O_3 and Cu/α-Al_2O_3 interfaces. As a result, the Nix-Freund model could quantitatively capture the flow stress of such epitaxial metal films. It was further observed that epitaxial film-substrate interfaces act as dislocation sources, and dislocation half-loops are emitted from the interfacial dislocation network. In contrast, no such phenomena have been observed in polycrystalline Al and Cu films deposited on amorphous oxide or nitride layers on Si substrates. The amorphous underlayers did not promote the formation of stable interfacial dislocation networks because they permitted atomic rearrangements at the interface, thus allowing for dislocation segments arriving at the interface to escape [14]. Consequently, in the absence of interfacial dislocations, the Nix-Freund or the Thompson model underestimated the flow stress in polycrystalline films deposited on amorphous layers [4,5] where initiation of plastic deformation is delayed due to the scarcity of dislocation sources.

Von Blanckenhagen et al. [15] used the aforementioned idea to model the deformation response of polycrystalline metal films. They considered dislocation sources in polycrystalline metal films to be rare and, therefore, each Frank-Read source inside a grain had to operate several times to generate more dislocations and achieve the resulting plastic deformation. Their

approach using discrete dislocation dynamics reproduced the experimentally measured flow stresses in polycrystalline Cu films deposited on amorphous and deformable polyimide layers. Thus, the underlying layer plays a major role in determining the plastic deformation of metal films: source controlled deformation models work well for polycrystalline films in the absence of interfacial dislocation networks, whereas epitaxially grown single crystal metal films are well described by the Nix-Freund model. However, there are hardly any studies on the deformation behavior of polycrystalline metal films grown epitaxially on polycrystalline layers. Although many metal films are deposited on amorphous diffusion barrier layers that are on top of single crystal silicon to prevent formation of metal silicides [16,17], there are cases when polycrystalline metal films were grown epitaxially on polycrystalline layers in order to achieve specific textures [18]. The deformation behavior of such films is expected to be significantly different than of those films deposited on amorphous layers. Furthermore, the Nix-Freund or the Thompson models which should be applicable to epitaxially grown metal films do not model the evolution of flow stress with plastic strain.

In this ARO-funded research program we investigated the plastic response of highly {111}-textured epitaxial polycrystalline Pt films grown on 35-50 nm thick (100)-textured polycrystalline rutile TiO_2 underlayers. We focused on relationships between the film thickness, grain size, and strain rate vs. the plastic mechanical response of textured Pt films with thicknesses ranging between 50-1000 nm in the form of bilayers with an underlying TiO_2 seeding layer. We also addressed the effect of the high aspect ratio columnar grain structure which was not captured by previous models. To this goal, we modified existing dislocation-based mechanistic models to account for strain hardening, in order to predict the evolution of flow stress with plastic strain and to compare with our experimental measurements.

III.A.1. Experimental Methods

Micro and nanometer thick Pt film specimens were fabricated at the US Army Research Laboratory (ARL) in Adelphi, MD using a combination of DC magnetron sputtering and etching on Si (100) substrate. Such Pt films are employed as contact electrodes in lead zirconate titanate (PZT) based Microelectromechanical Systems (MEMS) because they provide a sharp interface that suppresses interdiffusion of Pb and provide an excellent growth template for PZT thin films [19-21].

The fabrication process, described in detail in [19], began with the deposition of a base layer of Ti on a 500 ± 25 nm thermally grown SiO_2 layer on a silicon wafer to serve as an adhesion layer using DC magnetron sputtering with a 99.99% pure Ti target at 40˚C. The Ti films had a strong {0001} texture with the basal plane of the hexagonal close packed (HCP)

structure lying in the plane of the substrate. The Ti films were then converted to rutile through oxygen annealing for 30 min inside a tube furnace at 750˚C. The TiO_2 films had measured thicknesses of 35 nm and 50 nm and X-Ray diffraction studies showed (100) texture for TiO_2. Next, Pt was sputtered onto the TiO_2, with thicknesses of 1000, 500, 200, 100 and 50 nm at a substrate temperature of 500°C, as shown in step (A) in Figure 1(a). The resulting {111}Pt||(100)TiO_2 grain-to-grain heteroepitaxy has been established before for 100 nm thick Pt films [18,19] with the underlying (100)-textured TiO_2 acting as the seed layer for the growth of {111}-textured Pt.

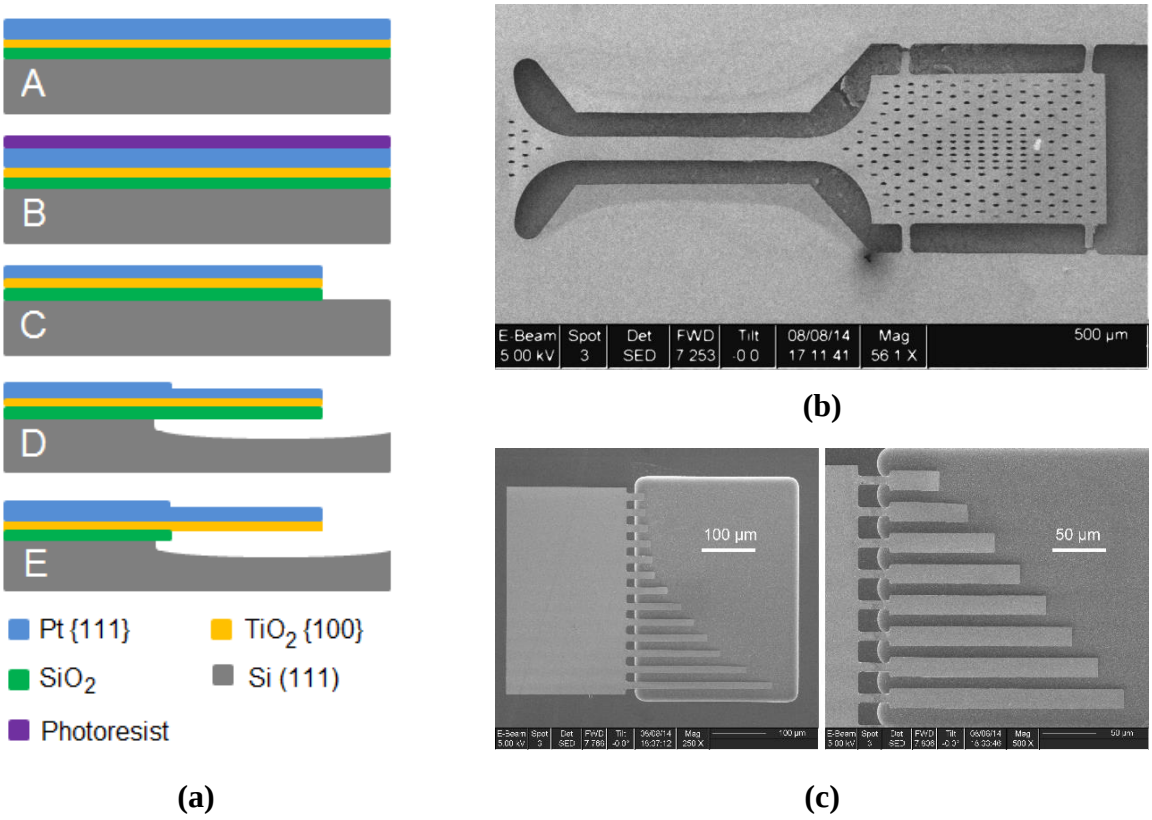

(a) **(b)** **(c)**

Figure 1. (a) Fabrication steps of freestanding Pt/TiO_2 specimens for mechanical experiments: (A) deposition of Pt by DC magnetron sputtering on TiO_2, (B) and (C) patterning via Ar ion milling, (D) etching of the underlying Si layer with XeF_2, and (E) removal of the SiO_2 layer via HF. **(b)** SEM micrograph of a dog-bone specimen for microscale tensile testing of 500-1000 nm thick Pt films. **(c)** SEM micrographs of micro-tensile specimens for mechanical testing of 50 – 200 nm thick Pt films. Note that the same specimen geometry as in (b) was used in microscale experiments with SiO_2, TiO_2-Pt, SiO_2-TiO_2-Pt, SiO_2-TiO_2-Pt-PZT and SiO_2-TiO_2-Pt-PZT-Pt-ALD stacks.

Patterning of the Pt films to specimen geometries and dimensions was done using Ar ion milling, as shown in steps (B) and (C). Prior to isotropic etching of the Si substrate to release the test structures, the wafer was exposed to 20-sec reactive ion etching with CHF_3 and O_2 to remove the surface oxide developed on the exposed silicon surfaces. Next, the film was subjected to xenon difloride (XeF_2) isotropic etching to remove the Si underneath as shown in step (D). Finally, freestanding Pt/TiO_2 bilayers were prepared by treatment with a solution of buffered hydrofluoric acid (HF) which removed the SiO_2 layer, step (E). After release, the wafer was diced to prepare individual dies containing dog-bone specimens with 1035 nm and 535 nm thicknesses, Figure 1(b), and micro-tensile specimens of 250 nm, 150 nm and 100 nm thickness, Figure 1(c). The dog-bone specimens had gauge width and length of 100 and 1000 μm, respectively, whereas the chosen micro-tensile specimens had three different gauge widths of 13, 19 and 30 μm, and lengths varied in the range of 150 - 350 μm.

A custom-built microscale tension apparatus for freestanding thin films, described in detail in [22], was employed to apply strain rates in the range of 10^{-6} to 10^{1} s^{-1}. Full-field strains were derived by application of Digital Image Correlation (DIC) to images of the specimen surface recorded with an optical microscope at frame rates as high as 30,000 fps. In order to compute strains, a random speckle pattern was deposited on the films by dispersing 1-μm Si particles [22].

III.A.2. Results and Discussion

Microstructure, Surface Morphology and Texture Characterization

Focused ion beam (FIB), scanning electron microscopy (SEM), atomic force microscopy (AFM) and X-ray diffraction (XRD) studies were conducted to determine the thickness, average grain size, surface morphology and texture of the Pt films, respectively. The mean grain size and standard deviation were measured from SEM micrographs, such as those shown in Figures 2(a-e), by using the intercept method. The unimodal curves in Figure 2(f) fit log-normal distribution functions well and broaden with increasing film thickness. The average planar grain size scaled with the Pt film thickness. Low current milling and cross-sectional imaging using a FIB revealed such columnar grains: Figures 3(a,b) show FIB-milled cross-sections of 1000 and 200 nm thick Pt films revealing a columnar grain structure approaching near-equiaxed shape.

XRD spectra showed highly {111}-textured Pt films with only {111} and {222} peaks for Pt. In addition to omega - 2theta scans, rocking curve measurements on {111} and {222} Pt peaks revealed {111}texture. The {222} full width at half maximum (FWHM) values between 1.5° and 2.3° indicate very good alignment of {111} planes parallel to the film surface. Finally,

pole figure analysis revealed {111} fiber texture with in-plane isotropy for all Pt films. Figures 3(c,d) show 2D pole figure plots for {111} planes in 1000 nm and 200-nm thick Pt films, respectively.

The surface morphology of the Pt film surfaces was investigated with AFM and average values for key surface roughness parameters were obtained at three different areas, each with dimensions 5×5 μm^2, 4×4 μm^2, 3×3 μm^2, 2.5×2.5 μm^2 and 2.5×2.5 μm^2 for 1000 nm, 500 nm, 200 nm, 100 nm and 50 nm films thick, respectively. Figure 4(a) shows the surface topography of a 5×5 μm^2 area in a 1000 nm thick film. Figure 4(b) shows the linear increase of the mean (Sa) and the root mean square (Sq) roughness of different film surfaces as a function of film thickness.

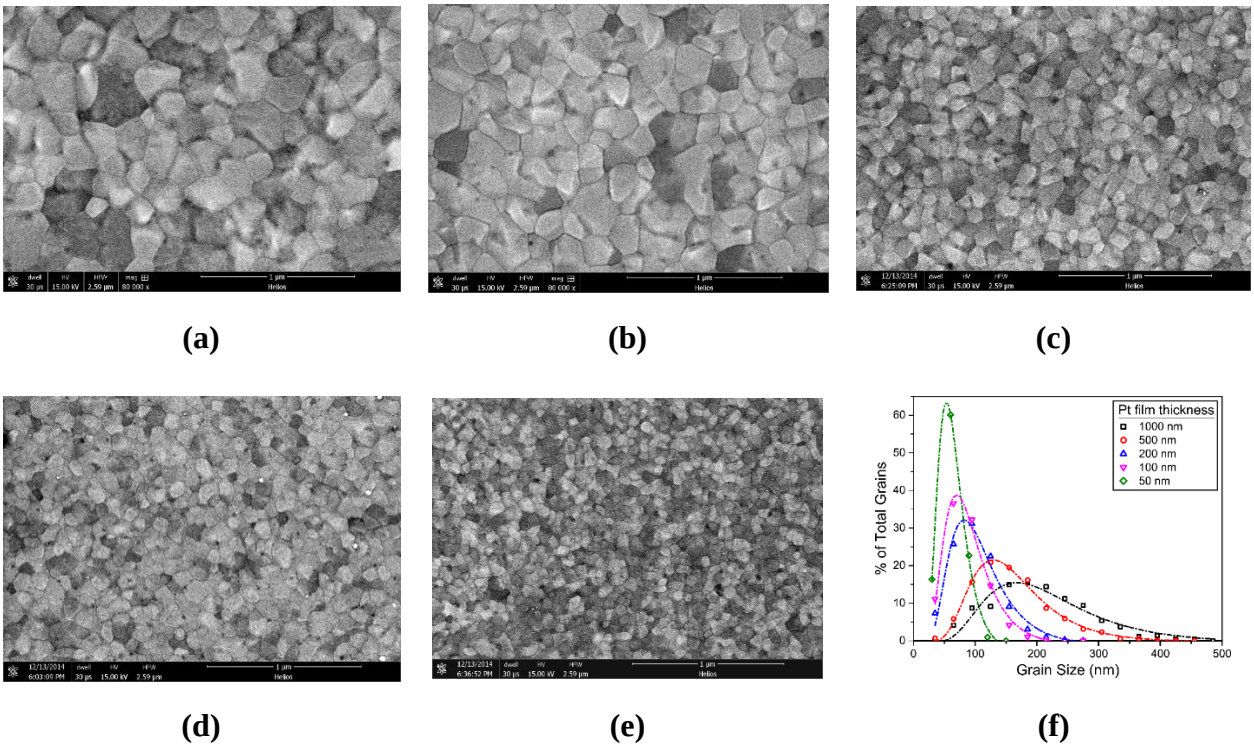

Figure 2. In-plane SEM micrographs of a **(a)** 1000-nm, **(b)** 500-nm, **(c)** 200-nm, **(d)** 100-nm, and **(e)** 50-nm thick Pt films. **(f)** The grain size distributions for the films shown in (a-e) obtained by the intercept method.

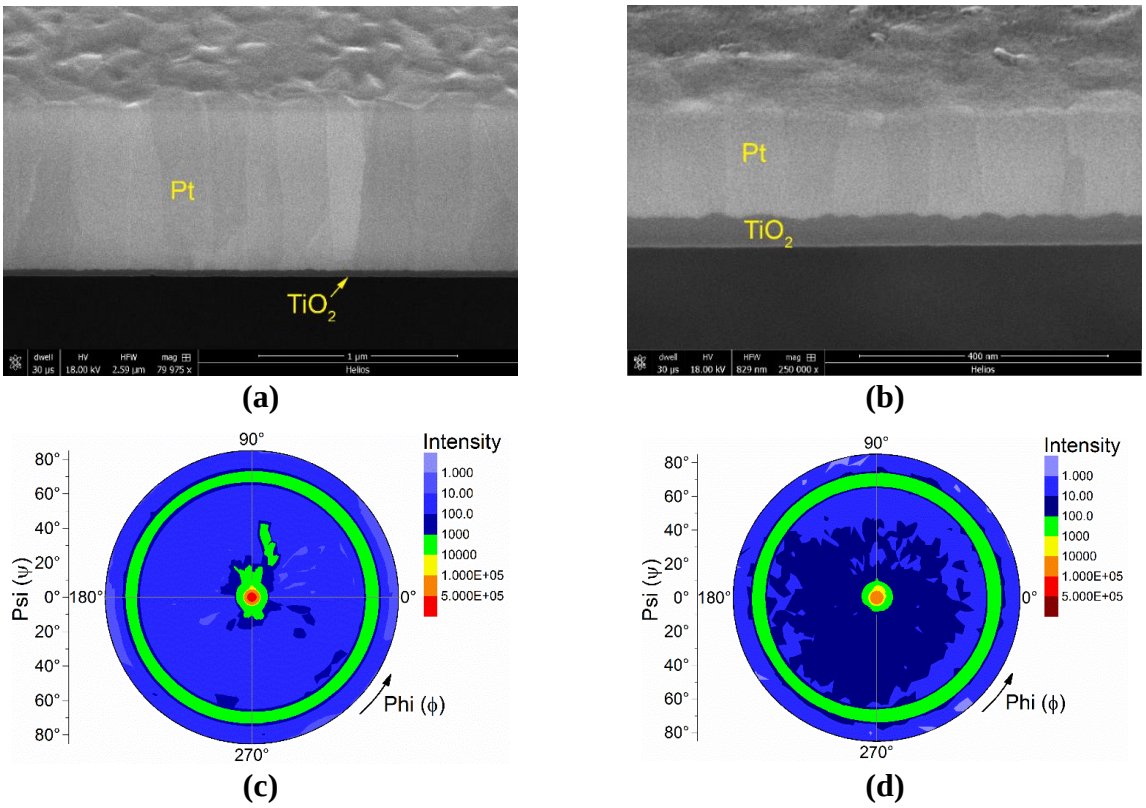

Figure 3. Columnar grains in **(a)** 1,000 nm and **(b)** 200 nm thick Pt films. 2D surface plots of pole figures of {111} planes for **(c)** 1000 nm and **(d)** 200 nm thick Pt films.

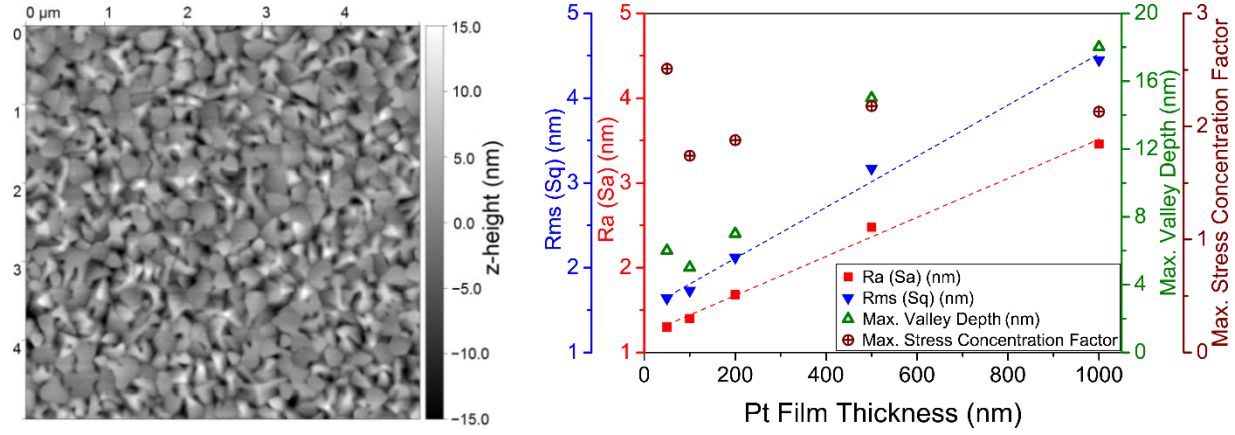

Figure 4. (a) Surface topography of a 1000-nm thick Pt film, and **(b)** surface roughness parameters: Sa, Sq, maximum valley depth and the computed maximum stress concentration factors (see later discussion) at the top film surface vs. Pt film thickness. The dashed line fits demonstrate a linearly increasing roughness with film thickness.

Elastic Properties of Pt and TiO_2 Films

Figure 5(a) shows the engineering stress vs. strain curves for Pt/TiO_2 bilayers tested at 10^{-3} s^{-1}. The elastic moduli were computed from the initial slopes of all stress vs. strain curves. The initial unloading moduli of Pt/TiO_2 bilayers were the same as the initial loading moduli. The Pt/TiO_2 bilayer modulus increased slightly with decreasing film thickness due to the contribution of the relatively higher modulus of TiO_2. The elastic moduli of the Pt and TiO_2 layers were extracted from the Pt/TiO_2 bilayer moduli by assuming isostrain deformation:

$$E_{Pt} = \frac{Ett_2{}' - E't't_2}{(t_1t_2{}' - t_1{}'t_2)} \tag{1a}$$

$$E_{TiO_2} = \frac{Ett_1{}' - E't't_1}{(t_1{}'t_2 - t_1t_2{}')} \tag{1b}$$

where E and E' are the elastic moduli of two Pt/TiO_2 bilayers with thicknesses t and t' respectively, t_1 and t_2 are the thicknesses of the Pt and TiO_2 layers, respectively, in the film with total thickness t, and $t_1{}'$ and $t_2{}'$ are the thicknesses of the Pt and TiO_2 layers, respectively, in the film with total thickness t'. Using Equations (1a) and (1b) and taking the average value of the elastic modulus for each Pt/TiO_2 thickness combination, the elastic moduli of Pt and TiO_2 films were computed as 167 ± 2 GPa and 195 ± 5 GPa, respectively.

The calculation of the theoretical values for the elastic moduli of polycrystalline (111)-textured Pt, $\overline{E}_{Pt}$ and (001)-textured TiO_2, $\overline{E}_{TiO_2}$ has been provided in Appendix A. $\overline{E}_{Pt}$ compares well with the experimental result of 167 ± 2 GPa, whereas there is a 15% difference between, $\overline{E}_{TiO_2}$, and the experimental result of 195 ± 5 GPa. The calculated elastic moduli values of the thin TiO_2 films are very sensitive to film thickness measurements. As inferred from the cross-sectional SEM micrograph in Figure 3(b), the interface between Pt and TiO_2 is rough, with the amplitude roughness accounting for a significant fraction of the thickness of the TiO_2 layer. For example, an overestimate of the thickness of the TiO_2 layer by 5 nm would result in 10% underestimate in the computed modulus of TiO_2.

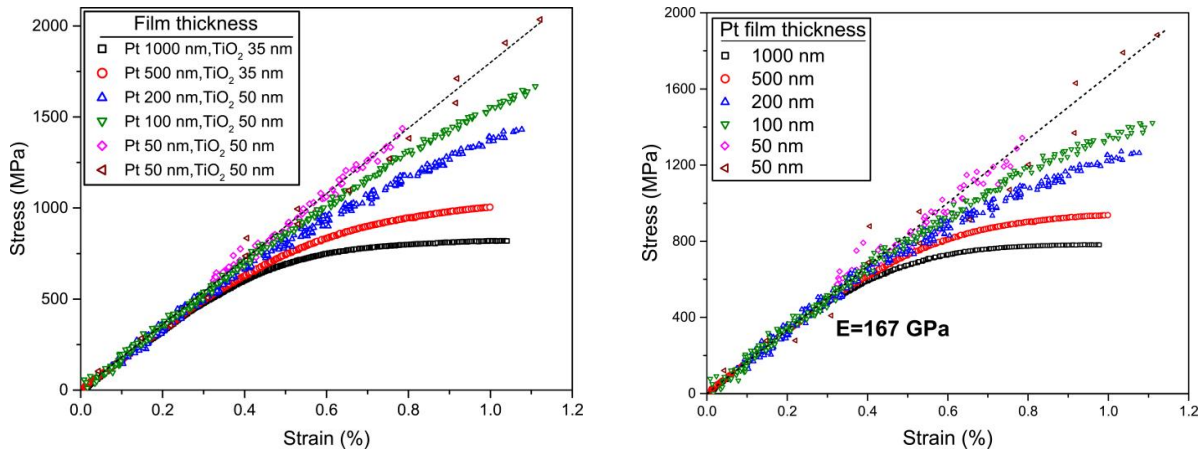

(a) **(b)**

Figure 5. (a). Engineering stress vs. strain response of freestanding textured Pt/TiO_2 bilayers. **(b)** Engineering stress vs. strain response of freestanding {111}-textured Pt films vs. film thickness, as extracted from (a). Note that two experiments for 50-nm thick Pt films are included in (a,b): while one specimen failed early (diamonds), the second specimen (triangles) failed roughly at similar strain as all other Pt/TiO_2 bilayer specimens.

Plastic Response of Pt Films

The stress vs. strain curves for the Pt films were extracted from the stress-strain response of Pt/TiO_2 films assuming that the Pt and TiO_2 layers are under the same strain and the total applied force, P_{total}, is partitioned between the two layers as P_{Pt} and P_{TiO_2}. The stress on the Pt layer is then obtained by subtracting the contribution of TiO_2 from the total applied force:

$$\sigma_{Pt} = \frac{1}{t_{Pt} w_{pt}} \left(P_{total} - P_{TiO_2} \right) \tag{2}$$

Equation 2 is valid as long as the TiO_2 layer remains elastic and the two layers remain perfectly bonded, even after Pt yielding. To this effect, the TiO_2 layer was inspected thoroughly and was found to be intact after specimen fracture, except very near to the region of specimen fracture. As a result, the deformation of the TiO_2 layer followed the Pt layer, and remained elastic until failure of the composite film. Figure 5(b) shows the stress vs. strain response of Pt films with different thicknesses as derived via Equation 2. Figure 6(a) shows the proportional limit and the 0.1% and 0.2% offset yield stress vs. the inverse Pt film thickness as extracted from Figure 5(b), following an increasing trend with decreasing Pt film thickness.

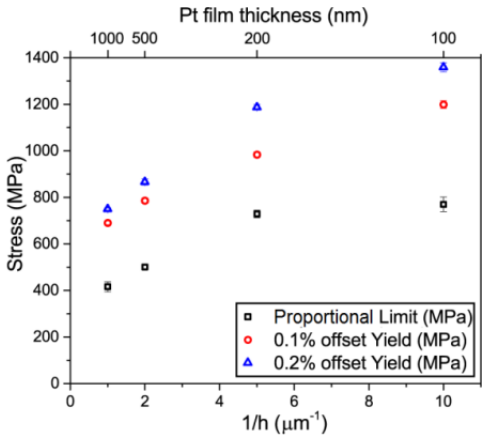

(a)

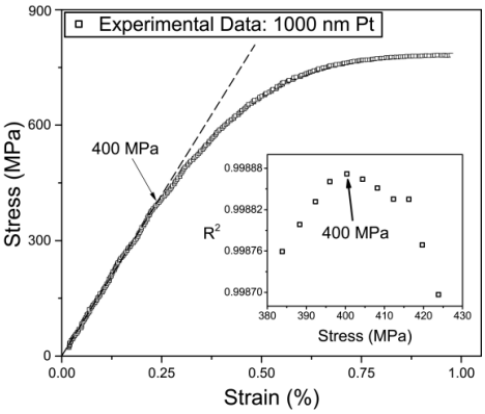

(b)

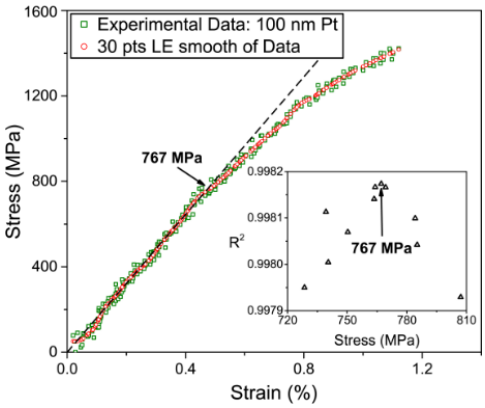

(c)

Figure 6. (a) Proportional limit, 0.1% and 0.2% offset yield stress vs. inverse Pt film thickness. Proportional limit of a **(b)** 1000 nm and **(c)** 100 nm thick film. Insets show the variation of the coefficient of determination, R^2, with stress, with the maxima corresponding to proportional limit values.

The proportional limit was determined by using as metric the value of the coefficient of determination, R^2, for the fitted regression line of the initially linear segment of the stress-strain curve. The effect of the addition of individual experimental datum points to R^2 was monitored near the region where deviation from linearity occurred, in order to determine the maximum value for R^2, as shown in the inset of Figure 6(b). The stress corresponding to maximum R^2 was identified as the proportional limit. The stress vs. strain data of 200-nm and 100-nm thick films, which demonstrated larger scatter compared to thicker films, were first smoothed by using the LOESS algorithm which utilized a local second-order polynomial regression by taking 30 points of a moving window. Subsequently, the proportional limit was determined by using the aforementioned R^2 approach, as shown in the inset in Figure 6(c) for a 100-nm thick Pt film. It should be noted that the proportional limit of many metals is the same, or slightly below, the elastic limit [23].

The elastic limit of a polycrystalline aggregate is the stress at which local plastic deformation is initiated; it can be estimated by using the most favorable condition for slip following Schmid's law for plastic yielding [24] which would begin in grains where the resolved shear stress exceeds the local critical resolved shear stress.

III.A.3. Model for Initiation of Plastic Deformation

For polycrystalline metal films grown epitaxially on polycrystalline underlayers, the mismatch strain at the interface with the underlayer gives rise to an interfacial dislocation network. Under tensile stress, dislocation loops are emitted from the interface and glide along slip planes in the metal film, eventually depositing segments at GBs and interfaces that act as impenetrable obstacles to dislocation motion. Emission of such dislocation half-loops from film/substrate interfaces has been experimentally observed before during *in-situ* thermal cooling of epitaxial single crystal Cu films [7]: The thermal tensile stresses generated in Cu films during cooling caused the loops to expand and eventually lay down dislocation segments at twin-boundaries and interfaces. At the critical shear stress, the work done by the tensile forces should be just enough to deposit the dislocation segments. The same idea was applied by Thompson to polycrystalline metal films bonded to rigid substrates with the exception that dislocations were considered to originate at defects at free surfaces of metal films rather than at the film/substrate interface. In particular, Thompson's model is applicable when the ratio of the in-plane columnar grain diameter to the grain height, d/h, is large, which applies to in-plane grain sizes that are roughly at least twice as large as the film thickness. Therefore, a modification to Thompson's model was necessary in the present study because **(a)** $d/h \leq 1$ for all Pt film thicknesses considered, **(b)** the TiO_2 substrate is not rigid, and **(c)** dislocations generally emanate from the

Pt/TiO_2 interface rather than the free film surface. The premise of the modified Thompson's model is that a dislocation network already exists at grain-to-grain heteroepitaxial $\{111\}Pt||(100)TiO_2$ interfaces because of 6.34% mismatch strain [18] between Pt and TiO_2. It is assumed that the Pt/TiO_2 interface acts as a source of dislocations, the generated dislocation loops subsequently grow in the presence of tensile stress and also create additional segments at GBs and interfaces. The modification of Thompson's model for $d/h < 1$ used in this work, described in detail in Appendix B, was adopted from Carel [25] who considered truncated ellipses instead of rectangles for the intersection of glide planes with cylindrical columnar grains. The modified Thompson's model predicts the elastic limit given by

$$\sigma_{elastic\ limit} \approx \frac{2.12}{Sb}(LW_{side} + d'W_{bottom}) \tag{3}$$

where S and b are the surface area of the glide plane and the Burgers vector of Pt, respectively. L and d' are the lengths of dislocation segments at the grain edge and the Pt/TiO_2 interface, respectively, and W_{side} and W_{bottom} are the energies per unit length of dislocation segments at the edge and at the interface of the grain, respectively. The plots in Figure 7(a) show good agreement between the predictions of the elastic limit by Equation 3 and the experimentally obtained proportional limit values for Pt films. It can be inferred from the experimental data that the proportional limit and the elastic limit of Pt are not much different. The solid lines are computed with Equation 3 as a function of film thickness and constant grain size using $\mu_f = 61\ GPa,\ \mu_s = 76\ GPa,\ \nu = 0.38,\ b = 2.76$ Å, and $\varphi = 70.5°$ for {111}-textured Pt. It must be noted that Equation 3 can only be used for $h \leq d\tan\varphi$. For $h > d\tan\varphi$, the glide plane starting from the film/substrate interface doesn't reach the top surface of the film. Therefore, the dashed lines are simple extrapolations beyond $h = d\tan\varphi$. Figure 7(b) shows the contributions of the two energy terms, W_{side} and W_{bottom}, to the elastic limit for films with 200 nm average grain size: the additive contribution of the two terms remains approximately constant beyond $h = d\tan\varphi$, because $d' \to 0$ as $h \to d\tan\varphi$, and L and S cannot increase further since the slip plane becomes confined inside the cylindrical grain as shown in inset (b) in Figure 7(b). Even if slip takes place along a parallel glide plane that does not start at the GB, inset (c), the elastic limit remains almost the same since the contribution of W_{side} will decrease but that of W_{bottom} will increase. As a result, dashed horizontal lines are drawn beyond $h = d\tan\varphi$ signifying that the elastic limit would remain unchanged with further increase in film thickness. This prediction is confirmed by the experimental proportional limit values for 1,000 nm and 500 nm thick films which fall on the dashed lines, as shown in Figure 7(a), while there is good agreement with the experimental proportional limit values for 200 nm and 100 nm thick Pt films.

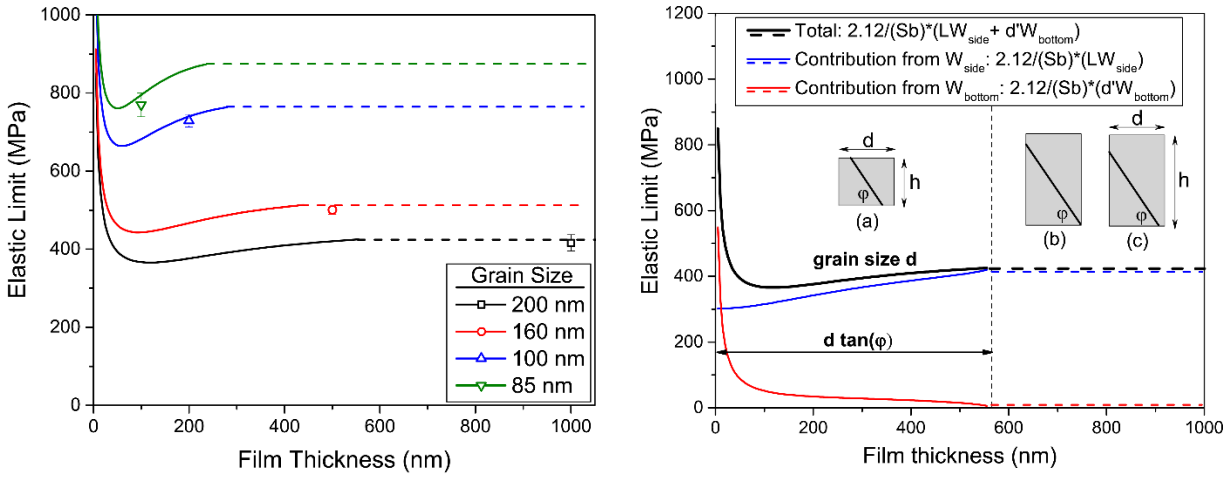

(a) **(b)**

Figure 7. **(a)** Elastic limit of Pt films as a function of film thickness. The solid lines are predictions by Equation 3. The dashed lines are extrapolations beyond $h = d\tan\varphi$ where h, d and φ are the film thickness, the grain size and the angle which a {111}-type glide plane makes with the interface respectively. The experimental values (symbols) of the proportional limit agree well with the model predictions. **(b)** Elastic limit (solid black line) vs. film thickness for films with 200 nm average grain size. Insets (a), (b) and (c) depict cylindrical columnar grains. Inset (a) falls within the region covered by existing theory whereas insets (b) and (c) show cases where the slip-planes do not reach the top film surface. The blue and red lines show the contributions of the two energy terms and are also extrapolated outside the region covered by theory.

III.A.4. Prediction of Plastic Flow Stress in Pt Films

Although, the modified Thompson model can describe the onset of yielding in textured Pt films with columnar grain-structure, it underestimates the 0.1% and 0.2% offset yield stress values because the dislocation density evolves during deformation. For instance, there is experimental evidence for dislocation proliferation with increasing plastic deformation in Cu films [6]. Increase in dislocation density leads to interactions among dislocations causing strain hardening which, in turn, increases the flow stress. However, the modified Thompson model takes into account the motion of a *single* dislocation loop and this underestimates the flow stress. Strain hardening as a result of interactions between gliding dislocations and arrays of stored dislocations depends on a number of factors which evolve with plastic strain, including density,

type and spatial distribution of dislocations. A rough estimate of the additional strengthening due to the presence of a non-zero dislocation density as a result of plastic deformation can be obtained by Taylor's equation:

$$\Delta\sigma = \alpha M \mu_f b \sqrt{\rho_T} \tag{4}$$

where α is a constant with values in the range 0.3 – 0.6, M = 3.67 is the Taylor factor for {111}-fiber texture [26], and ρ_T is the average dislocation density. The latter may be represented as a combination of the density of geometrically necessary dislocations (GND) and the statistically stored dislocations (SSD).

GNDs are stored at GBs during deformation to relax incompatibility stresses in adjacent grains. Following the work by Ashby [27], the density of GNDs as a function of plastic strain is given by

$$\rho_{GND} = \frac{N\varepsilon_{plastic}}{bd} \tag{5}$$

where $\varepsilon_{plastic}$ is the plastic strain and N = 2 for a two-dimensional columnar grain structure. The density of SSDs is difficult to be analytically derived. There are several dislocation sources in a material, which may act independently or in a coordinated manner during deformation to increase the density of SSDs, e.g. *Frank-Read* sources or GB ledges may act as dislocation sources [28] to create a network of dislocations during plastic deformation, thus increasing the density of SSDs in each grain. For simplicity, it is assumed that at small length scales the two dislocation densities are comparable, $\rho_{GND} \sim \rho_{SSD}$ [29]. Therefore, the total average dislocation density is given by

$$\rho_T = \rho_{GND} + \rho_{SSD} = \frac{2N\varepsilon_{plastic}}{bd} \tag{6}$$

A similar approach was adopted by Hommel and Kraft [6] who inferred from an X-ray FWHM analysis the total dislocation density as a function of grain size and plastic strain in 1 μm thick Cu films deposited on a polyimide substrate. It may be noted that Equation 6 does not have any material parameters except for the Burgers vector which does not vary much for FCC metals. A good agreement has been confirmed between the dislocation densities predicted by Equation 6 and those measured in Cu by Hommel and Kraft [6], and as a result, the same equation is used here to predict the average dislocation density in Pt films vs. plastic strain and grain size.

Adding the stress increment due to the Taylor strain hardening mechanism given by Equation 4 to the stress required to initiate plasticity given by the modified Thompson model in Equation 3, the total flow stress becomes:

$$\sigma_{flow} = \sigma_{elastic\ limit} + \alpha M \mu_f b \sqrt{\rho_T} \approx \sigma_{elastic\ limit} + \alpha M \mu_f \sqrt{\frac{2Nb\varepsilon_{plastic}}{d}} \quad (7a)$$

$$\sigma_{flow} \approx \sigma_{elastic\ limit} + \frac{k(\varepsilon_{plastic})}{\sqrt{d}}; where\ k(\varepsilon_{plastic}) = \alpha M \mu_f \sqrt{2Nb\varepsilon_{plastic}} \quad (7b)$$

The evolution of flow stress with plastic strain as predicted by Equation (7a) can be verified by fitting it to the experimental stress vs. plastic strain data: Figure 8 shows a moderately good quantitative agreement for different film thicknesses for $\alpha = 0.47$. It may be noted that, for the thicker films, Equation 7 overestimates the flow stress beyond 0.2 % plastic strain. This may be due to the lack of an inbuilt recovery process in the model such as dislocation annihilation.

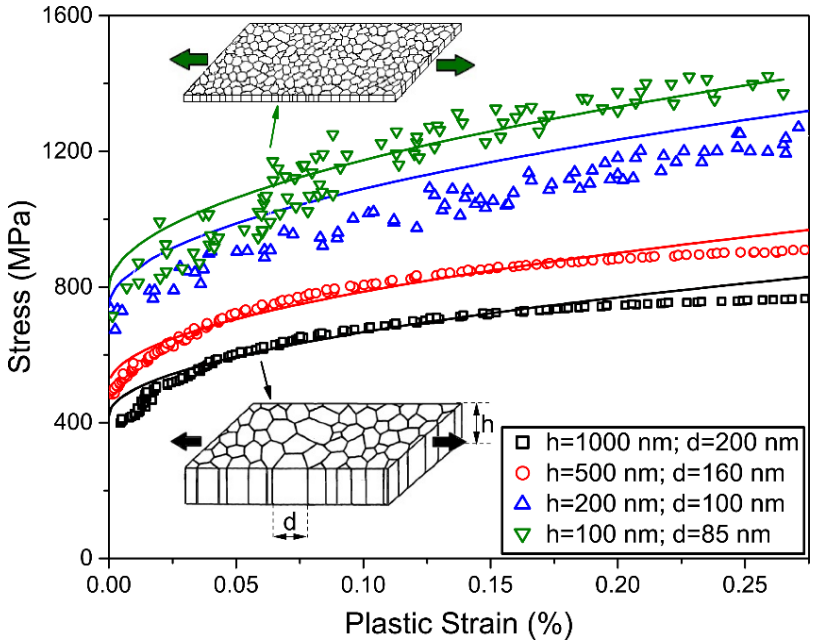

Figure 8. Experimental flow stress vs. plastic strain for Pt films. The prediction of our model is represented by the solid lines with good agreement with experiments (symbols). The schematic provides the definition of the geometrical parameters. The lowermost curve corresponds to the thickest film with the largest grain size, whereas the uppermost curve corresponds to the thinnest film with the smallest grain size. Note that the grain size and film thickness were not controlled independently, therefore their effect on the experimentally determined mechanical behavior of Pt films was coupled, and an appropriate model, such as this developed in this research program, was required to capture their combined effect.

Equation (7a) can been rewritten as Equation (7b) to emphasize that the strain hardening model reduces to the Hall-Petch grain-size strengthening model with the Hall-Petch coefficient becoming a function of plastic strain. This approach of obtaining the Hall-Petch slope by removing the grain size dependent term from the dislocation density function is also found in a study by Hansen [30]. The value used for the single fitting parameter $\alpha = 0.47$ in Equation (7a) is justified if the Hall-Petch coefficient calculated by Equation (7b) for 0.2% plastic strain agrees well with the literature data: Specifically, the Hall-Petch coefficient $k(\varepsilon_{plastic})$ computed for 0.2% plastic strain of Pt films is 0.16 $MPa\sqrt{m}$ which compares well with the value of 0.18 $MPa\sqrt{m}$ reported in literature [31].

III.A.5. Strain Rate Sensitivity of Pt/TiO_2 Films

Notably, the strain at failure was consistent (~1%) for Pt/TiO_2 films of different thickness but the plastic strain at failure decreased with decreasing Pt film thickness: Computed from the data in Figure 5(b), the plastic strain accumulated in 1,000 nm, 500 nm, 200 nm, 100 nm and 50 nm thick Pt films, was 0.5%, 0.4%, 0.3%, 0.25% and ~0%, respectively. Figures 9(a-c) show the fracture profiles of 1,000 nm, 500 nm and 100 nm thick Pt films. Figure 9(d) shows strain localization in a 1,000 nm thick film, whereas 500 nm thick films demonstrated intergranular cleavage, as shown in Figure 9(e). Figure 9(f) shows that cracks in the TiO_2 layer formed only near the bilayer fracture zone while the rest of the TiO_2 layer remained crack-free until specimen failure. This result supports the use of isostrain and elastic behavior for the TiO_2 layer in computing the strain in Pt by Equation 2.

The failure of 1,000 nm and 500 nm thick films was controlled by the Pt layer. The failure mechanism in the thicker films can be understood by considering the grain size distribution of Pt. For broad grain size distributions, small grains have higher yield strength compared to larger grains, resulting in non-uniform local deformation. Compared to thinner films, the 1,000 nm thick Pt films had much broader grain size distribution and larger mean grain size. Under tension, strain localized in the larger grains which allowed for development of plastic deformation in regions of maximum shear. Evidence for this process is shown in Figure 9(d).

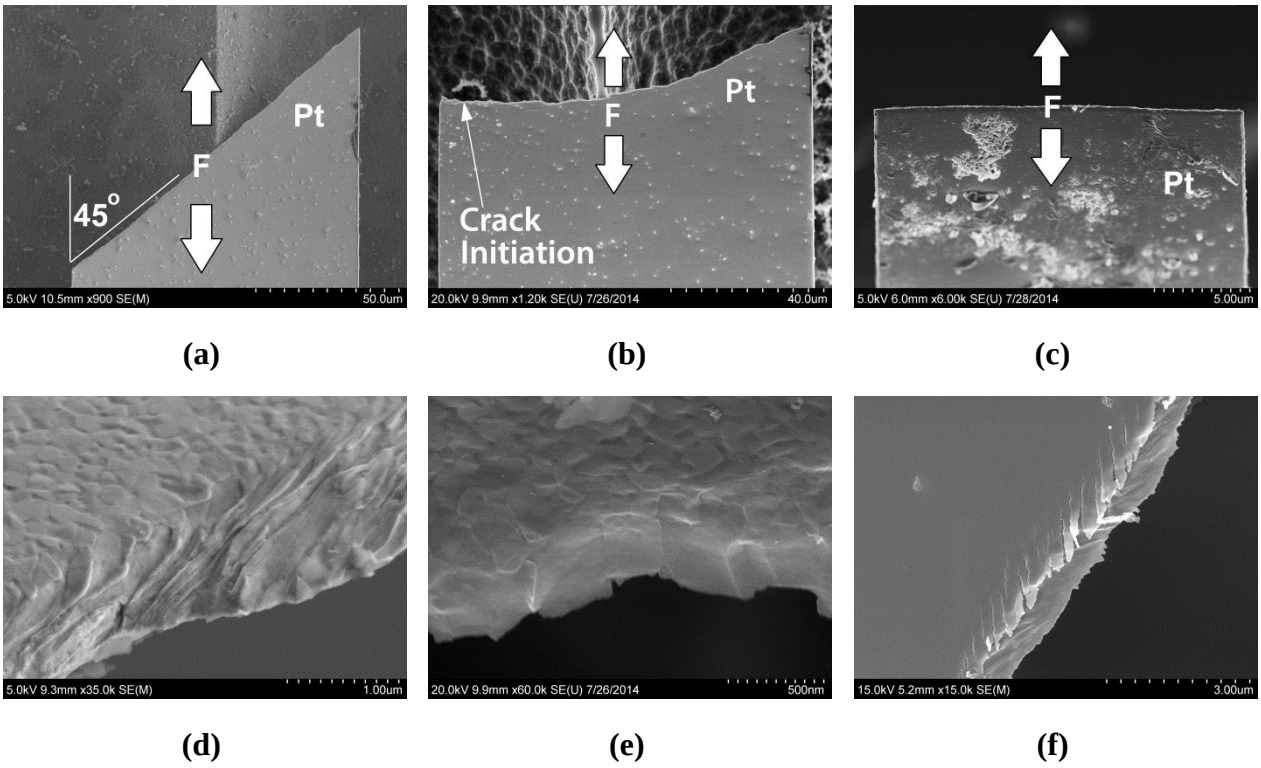

(a) **(b)** **(c)**

(d) **(e)** **(f)**

Figure 9. Fracture profiles of Pt specimens with **(a)** 1,000 nm, **(b)** 500 nm, and **(c)** 100 nm thickness. The loading direction is denoted by the arrows. **(d)** Strain localization in a 1,000 nm thick specimen. **(e)** Intergranular cleavage of a 500 nm thick specimen. **(f)** Cracks in the TiO_2 layer very near to the fracture surface of the Pt/ TiO_2 bilayer, while the rest of the TiO_2 layer was damage-free.

Such a mechanism for strain localization is strain rate dependent. Figures 10(a,b) show engineering stress vs. strain curves for 1,000 nm and 500 nm thick Pt films subjected to tensile strain rates between 2×10^{-6} s^{-1} and 6 s^{-1}. Notably, in this range of strain rates, the failure strain increased with increasing strain rate by as much as 30%, which is not typical for metals. Such an anomalous behavior may occur due to more uniform plastic flow with increased strain rate as a result of suppression of strain localization and increased small scale yielding taking place at high strain rates. This was argued before by Rupert [32] based on molecular dynamics simulations of nanocrystalline Ni. Post-mortem fracture surface imaging supports this argument as shown in Figures 10(c,d) where increased strain localization at slower strain rates led to smaller engineering strains. However, the yield stress increased only slightly with strain rate. The strain rate sensitivity of 1,000 nm thick Pt films was low, ~0.01. Such small values would promote strain localization as observed experimentally. The 500 nm thick Pt films showed further reduced sensitivity to strain rate with the yield stress remaining practically unchanged.

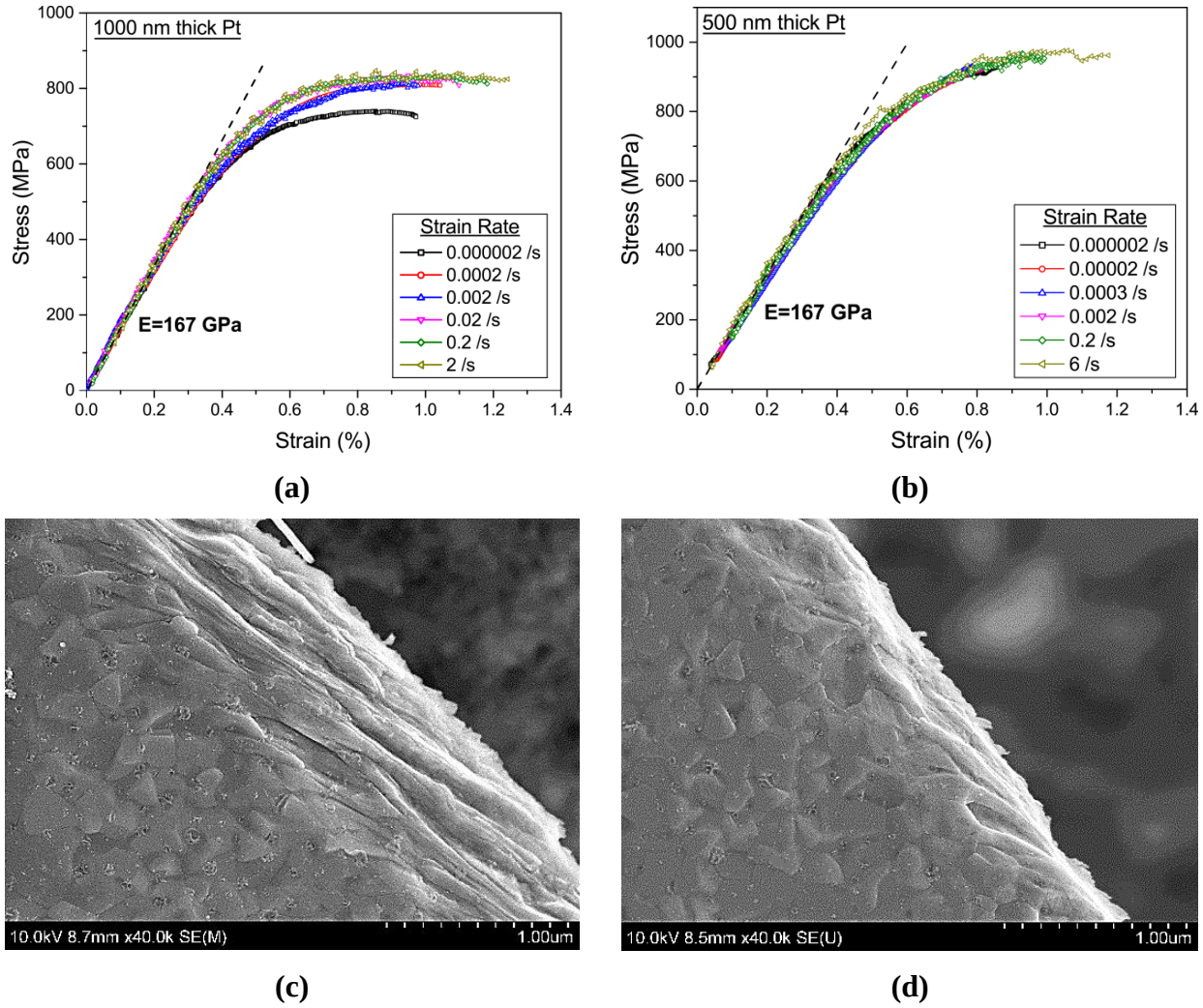

Figure 10. Engineering stress vs. strain curves for **(a)** 1,000 nm and **(b)** 500 nm thick Pt films subjected to various strain rates. Strain localization in 1,000 nm thick Pt films, tested at the **(c)** strain rate of 10^{-6} s^{-1}, and **(d)** 10^{-2} s^{-1}.

A reduction in Pt film thickness resulted in narrower grain size distribution and decreased mean grain size, which, in turn, impacted plastic deformation: 50 nm thick Pt films demonstrated brittle fracture, which may be due to a change in deformation mechanism from full to partial dislocations as reported before for Al [33], Au [34] and Ta/Cu [35] films with thicknesses in the range of 40-100 nm. The stress required to nucleate partial dislocations accompanying a stacking fault are smaller than those required to full dislocations when the grain size or film thickness falls below a critical size. The resulting partial dislocations are harder to cross-slip and provide an additional constraint to dislocation motion.

III.A.6. Summary of Results from Studies with Highly Textured Pt Films

The effect of film thickness and grain size on the mechanical response of freestanding nanocrystalline {111}-textured Pt films, which were epitaxially grown on rutile TiO_2 seed substrates with columnar grain structure, was experimentally and analytically investigated for Pt/TiO_2 bilayer films with thicknesses in the range of 100 to 1000 nm. The measured elastic modulus of Pt (E_{Pt}=167 ± 2 GPa) agreed well with theoretical estimates for the in-plane modulus of {111}-textured polycrystalline Pt, while the modulus of TiO_2 (E_{TiO_2}=195 ± 5 GPa) was 15% lower than the theoretical estimate for (100)-textured polycrystalline TiO_2. The flow stress of Pt/TiO_2 films increased with reduced thickness. The experimentally determined proportional limit of Pt was consistent with predictions by a modified Thompson model for plastic deformation of polycrystalline columnar metal thin films. However, the yield stress was underestimated by the same model and a Taylor strain hardening model was superimposed to the modified Thompson model to account for additional hardening occurring as a result of dislocation interactions during plastic deformation. The combined model, which is also a Hall-Petch grain strengthening model, predicted well the evolution of flow stress with plastic strain.

III.B. Mechanical and Ferroelectric Properties of Freestanding PZT Films with Texture

PZT films are used in many microelectromechanical systems (MEMS) [36-39]. Perovskite ferroelectric materials are strongly anisotropic, therefore, control of their grain orientation is critical for improved electromechanical properties [40] and enhanced low voltage actuation. Several studies [40,43] have reported improved piezoelectric coefficients, $e_{31,f}$ and $d_{33,f}$ of {100} oriented polycrystalline PZT films at the morphotropic phase boundary (MPB), demonstrating that the intrinsic response of PZT associated with ionic deformation of unit cells depends on texture. There has been recent focus on orientation control of polycrystalline PZT films and thus, their piezoelectric and dielectric properties [44-48]. However, few studies [49-52] have probed the dependence of the mechanical properties on film texture with good control of the latter. Prior studies using various techniques [49-55] have reported a broad spectrum of values for the elastic modulus, ranging from 37 GPa [56] to 400 GPa [57], with major implications on the calculation of other fundamental properties. The determination of the piezoelectric strain coefficient, d_{31}, requires explicit knowledge of the elastic modulus [58-60]. Large inaccuracies of the latter directly translate into the wide disparities in d_{31} values reported in literature in the range 30-180 pmV^{-1} [61,62]. Furthermore, there are no prior studies relating the effect of texture on the d_{31} coefficient and on the ferroelasticity of freestanding PZT films. This research program addressed the lack of quantitative information about the open circuit elastic and ferroelastic behavior and transverse piezoelectric coefficient, d_{31} of polycrystalline PZT films as a function of texture, with measurements conducted on freestanding PZT film stacks. PZT (52/48) films with 0-10% excess Pb were deposited on $PbTiO_3$ seed layers with 0-30% excess Pb. The excess Pb in the $PbTiO_3$ layer in conjunction with the texture of the underlying Pt film controlled the PZT texture. Although (111) and (100) textured PZT films have been fabricated in the past [63,64], it has not been possible to control their texture without modifying the seeding layer [43,48]. Furthermore, in prior studies the PZT films were bonded to thick Si substrates, which prevented the direct measurement of their mechanical behavior and required precise knowledge of the mismatch stresses [65,66].

The present PZT films were implemented as composite stacks forming d_{31} type actuators. The stacks had an elastic SiO_2 layer, TiO_2 adhesion layer, Pt metallization layer, PZT(52/48) layer, another Pt metallization layer, and finally an ALD layer consisting of Al_2O_3 and HfO_2. The measured thicknesses of the SiO_2, TiO_2, bottom Pt, top Pt, and ALD layers were 300 nm, 35 nm, 100 nm, 50 nm and 75 nm, respectively. The entire stacks were of the sequence SiO_2-TiO_2-Pt-PZT-Pt-ALD. Combinations, such as TiO_2-Pt, SiO_2-TiO_2-Pt, SiO_2-TiO_2-Pt-PZT and SiO_2-TiO_2-Pt-PZT-Pt-ALD were tested in uniaxial tension to deduce the properties of each layer and compute the Young's modulus of the PZT films with different textures under open circuit conditions. The transverse piezoelectric coefficient, d_{31}, was measured from the out-of-plane

displacement of unimorph SiO_2-TiO_2-Pt-PZT-Pt cantilevers which were subjected to triangular waveform electric field.

III.B.1. Experimental Methods

PZT-based MEMS devices were fabricated at the US Army Research Laboratory (ARL) in Adelphi, MD, using chemical solution deposition [67]. A highly {111} textured 100 nm Pt layer was deposited by magnetron sputtering onto a 35-nm highly {100} textured TiO_2 film that was grown on 300 nm thick SiO_2. Then, 20 nm $PbTiO_3$ seed layers containing 0-30% Pb-excess were prepared using the 2-Methoxyethanol (2-MOE) synthesis route. PZT(52/48) solutions with 0-10% Pb-excess were then spun-cast and pyrolyzed on the $PbTiO_3$ seed layers according to the 2-MOE synthesis route, similarly to the solution preparation method by Budd *et al*. [68]. The total thickness of the pyrolyzed PZT was ~500 nm. Following the PZT deposition, a 50-nm top Pt electrode was sputtered and patterned using Ar ion milling, followed by a second Ar ion-milling to pattern the PZT layer. Next, a combination of Ar ion milling followed by wet etching was used to pattern the PZT layer and open access to the bottom Pt electrode. Then, a 60 nm layer of Al_2O_3 and a 15 nm layer of HfO_2 were deposited by atomic layer deposition (ALD). These layers were then patterned via fluorine plasma-based reactive ion etching to open access to the bottom and top Pt electrodes. Next, reactive ion etching (RIE) via fluorine plasma was performed on the elastic layer, which enabled access to the Si substrate for the final release step. The entire wafer was placed in a XeF_2 etching chamber for isotropic etching of the exposed Si, thus creating freestanding dog-bone specimens for mechanical testing. The microscale dog-bone specimens were 1000 μm long, 100 μm wide and ~1 μm thick. SEM/FIB and XRD studies were conducted to determine the thickness and texture of the PZT stacks. The thicknesses of the PZT layers and the in-plane grain size of the PZT films are provided in Table 1. Henceforth, the each type of film is referred to by the sample number given in Table 1.

The custom-built apparatus for microscale uniaxial tension experiments with freestanding dog-bone shaped Pt films, Figure 1(b), was employed to test the microscale PZT-based specimens under an optical microscope and at 10^{-4} s^{-1} strain rate [22]. The full-field 2D film strains were computed via DIC from high magnification optical images of the film surface, which were recorded during testing. A random speckle pattern was deposited on the film surface by dispersing 1-μm Si particles to facilitate the calculation of film strain [22], while the applied force was measured using a loadcell with 0.5 N maximum force capacity.

For the measurement of the transverse piezoelectric coefficient, d_{31}, triangular waveform voltage profiles of 0-10 V were applied to SiO_2-TiO_2-Pt-PZT-Pt cantilevers between the upper

and bottom Pt electrodes, and the out-of-plane displacements were measured at several locations along the cantilevers using a laser Doppler vibrometer and a laser interferometer. The frequency of the triangular waveform signal was 2 Hz which was much less than the resonance frequency of the cantilevers.

Table 1. Thickness of PZT layers in SiO_2-TiO_2-Pt-PZT stacks and percentage of texture factors.

Sample#	%Pb-excess $PbTiO_3$	%Pb-excess PZT	PZT Thickness (nm)	PZT in-plane grain size (nm) [67]	% T_{001}	% T_{110}	% T_{111}
6117	0	0	500	-	21	20	59
6109	0	3	520	74 ± 2	44	17	39
6101	0	5	540	125 ± 3	15	15	70
6103	0	10	500	-	9	23	68
6006	10	3	520	79 ± 2	0	0	100
6015	10	5	550	79 ± 2	19	0	81
6017	20	3	520	73 ± 4	0	0	100
6155	20	5	520	111 ± 2	25	18	57
6001	20	8	550	121 ± 1	78	22	0
6113	30	3	525	-	73	0	27
6019	30	5	525	103 ± 2	100	0	0
6020	30	8	505	93 ± 2	100	0	0
6122	30	10	525	84 ± 3	59	0	41

Texture Characterization

Figure 11 shows X-ray 2theta-omega scans for samples #6006, #6109 and #6020. Sample #6006 and #6020 show only (111) and (001) PZT peaks, respectively. Sample #6109 shows (001), (110) and (111) peaks. In addition to 2theta - omega scans, rocking curve

measurements revealed preferred (001), (110) and (111) textures with FWHM values for (001), (110) and (111) peaks ≤5˚, ≤3˚ and ≤8˚, respectively. Pole figure plots revealed fiber texture.

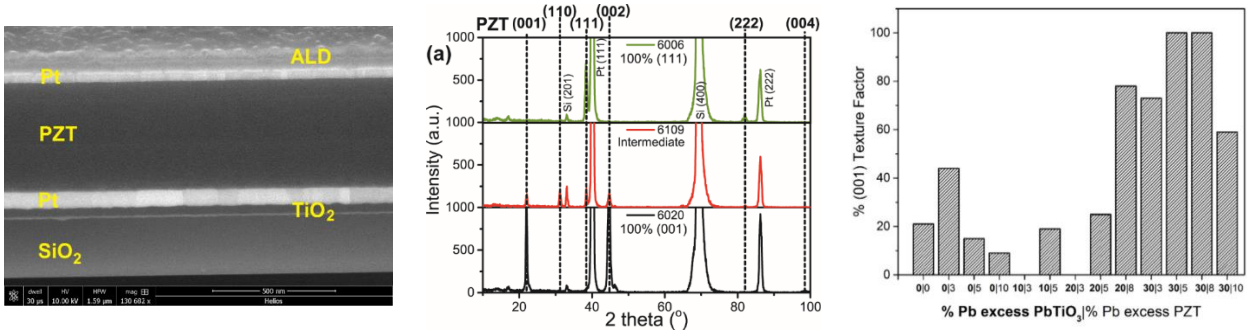

(a) **(b)** **(c)**

Figure 11. **(a)** Cross-section of sample #6019 showing the layers of a SiO_2-TiO_2-Pt-PZT-Pt-ALD stack. **(b)** XRD plots showing (100), (110) and (111) texture of three different PZT films. **(c)** (001) texture factor vs. excess Pb. Separated by a vertical bar in the x-axis labels is the excess Pb percentage in the $PbTiO_3$ and the PZT layer.

XRD was used to quantify the degree of preferred orientation by comparing the integrated intensities of the thin film θ/2θ diffraction pattern with those of a powder sample [69]. The integrated intensities of a powder sample were obtained from the standard PDF#01-070-4060 from the International Centre for Diffraction Data. Since three preferred orientations were present, three percentage texture factors were evaluated according to [69] as a measure of the degree of enhancement or reduction in the *hkl* reflection due to preferred orientation, compared to a powder sample. For example, the %(001) texture factor is calculated according to:

$$\%\, T_{001} = \frac{\frac{I^F_{001}/A_{\theta 2\theta}(\theta_{001})}{I^{ICDD}_{001}}}{\left(\frac{I^F_{001}/A_{\theta 2\theta}(\theta_{001})}{I^{ICDD}_{001}} + \frac{I^F_{110}/A_{\theta 2\theta}(\theta_{110})}{I^{ICDD}_{110}} + \frac{I^F_{111}/A_{\theta 2\theta}(\theta_{111})}{I^{ICDD}_{111}}\right)} \tag{8}$$

where I^F_{hkl} is the integrated intensity for diffraction from a *hkl* plane in a thin film, I^{ICDD}_{hkl} is the integrated intensity for diffraction from the same *hkl* plane in a standard random powder, and $A_{\theta 2\theta}(\theta_{hkl})$ is the absorption factor [69] at the Bragg angle θ_{hkl}. The calculated percentage texture factors are listed in Table 1 by using a linear absorption coefficient value $\mu_{PZT} = 1325$ cm^{-1}. In general, an increased value of excess Pb in the $PbTiO_3$ seed layer resulted in increased (001) texture, Figure 11(c), as also reported in [47].

Mechanical Characterization

Uniaxial tension experiments were performed to extract the elastic modulus of the individual layers in PZT stacks. The elastic moduli of the TiO_2 and Pt layers were reported in [70] and the mechanical response of the SiO_2-TiO_2-Pt composite stack was found to be perfectly linear until failure at 0.85% strain. The stress-strain response of all SiO_2-TiO_2-Pt-PZT stacks was non-linear, with the degree of non-linearity increasing with (001) texture. Since the SiO_2-TiO_2-Pt films were perfect linear, this non-linearity was due to the mechanical behavior of textured PZT layers. The stress-strain response of textured PZT (52/48) layers was extracted from the SiO_2-TiO_2-Pt-PZT response, Figure 12(a), by subtracting the contribution of the SiO_2-TiO_2-Pt stack assuming isostrain conditions between all layers. Figure 12(b) shows a magnified portion of the PZT stress-strain curves illustrating the effect of texture on the elastic modulus of PZT. Additionally, open circuit tensile tests performed on SiO_2-TiO_2-Pt-PZT-Pt-ALD stacks reproduced the same effect of texture on modulus. By subtracting the contribution of the SiO_2-TiO_2-Pt-PZT stack from the stiffness of the entire SiO_2-TiO_2-Pt-PZT-Pt-ALD stack, the effective modulus of Pt-ALD layers was found to be 162 ± 21 GPa which resulted in an ALD modulus of 159 GPa, close to the value of 150-155 GPa reported for ALD-deposited Al_2O_3 [71].

Figure 12(a) shows that (001) textured PZT exhibit the most non-linearity, compared to the least non-linearity of (111) textured PZT. This non-linearity of thin film [53] and bulk PZT [72,73] at the morphotropic phase boundary (MPB) has been attributed to stress-induced ferroelastic 90˚ domain switching in the tetragonal phase. Ferroelastic domain switching in PZT ceramics at the MPB can be very complicated. A simple analytical micromechanics model based on Eshelby's inclusion problem [74,75] (Appendix C) was adapted to the film textures in this study to compute the strain due to domain switching by accounting for tetragonal symmetry. For (001) texture, *c* domains switch to a_1 or a_2 domains in grains whose (001) and (010) axes, respectively, are aligned with the loading axis, Figure 12(c) inset (i), to minimize the overall energy of the system. Similarly, 90˚ switching takes place for (111) texture, for example from d_3^- to d_1^+ domains, as shown in Figure 12(c), inset (ii). Finally, the induced strain from domain switching is added to the elastic strain to compute the total strain at any given stress:

$$\varepsilon_{total_{(001)}} = \frac{\sigma}{E_{(001)}} + \frac{15(1-\nu^2)}{2E_{(001)}(7-5\nu)}\left(\sigma - \sigma_{th_{(001)}}\right) \tag{9a}$$

$$\varepsilon_{total_{(111)}} = \frac{\sigma}{E_{(111)}} + \frac{15(1-\nu^2)}{2E_{(111)}(7-5\nu)}(0.5774^2)\left(\sigma - \sigma_{th_{(111)}}\right) \tag{9b}$$

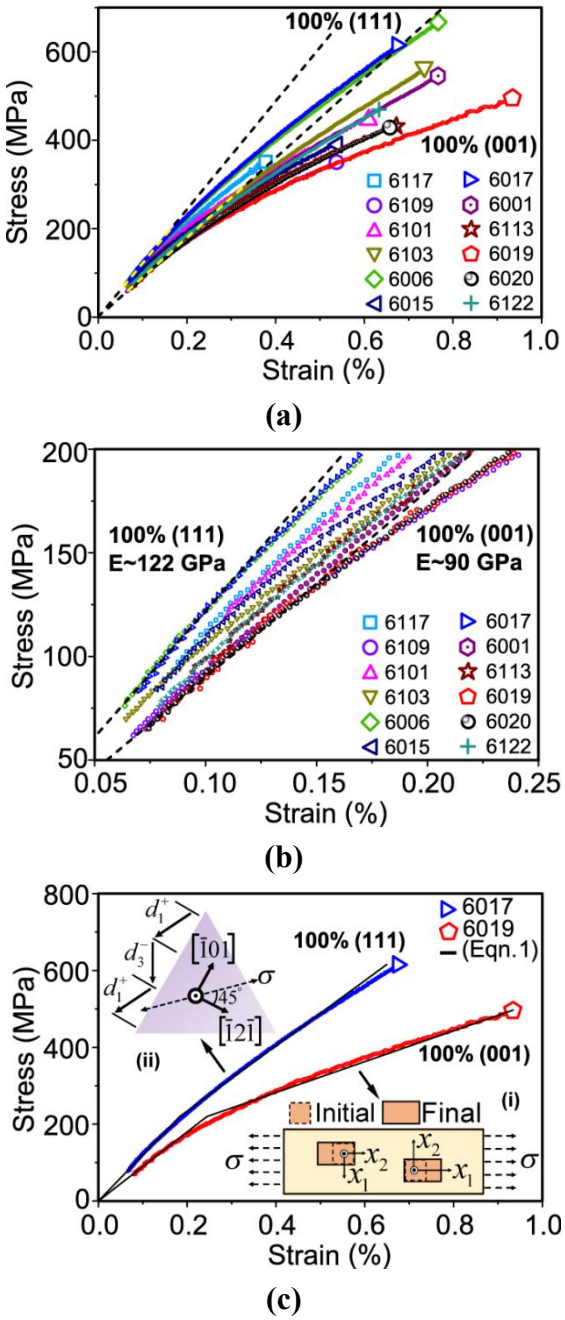

Figure 12. Calculated stress vs. strain response of **(a)** PZT films with various textures using the experimental measurements from SiO_2-TiO_2-Pt-PZT composite films. **(b)** Magnified region of the stress vs. strain curves in (a), showing the initial PZT stiffness as a function of texture. **(c)** Comparison between analytical model and experimental results: Inset (i) shows the top view of a (001) textured PZT film. The crystallites oriented along the stress direction undergo preferential domain switching (c-a_1) and (c-a_2) giving rise to a non-linear stress vs. strain response; Inset (ii) shows the (111) plane and a uniaxial stress applied in [-(1+√3) 2 (-1+√3)] direction when d_3^- domains switch to d_1^+ domains, resulting in non-linear mechanical behavior.

where $E_{(001)}, E_{(111)}, \nu, \sigma$ and σ_{th} are the elastic moduli for (001) and (111) texture, the Poisson's ratio ($\nu = 0.3$), the applied stress and the threshold stress for 90˚ domain switching, respectively. Figure 12(c) shows that Equations (9a) and (9b) fit well the experimental stress-strain responses for $\sigma_{th_{(001)}} = \sigma_{th_{(111)}} = 220$ MPa and the fractions of 90˚ domain switching equal 10% and 17% for (111) and (001) texture, respectively. The enhanced hysteresis and the associated increase in the computed fraction of 90˚ domain switching in (001) films provide proof that ferroelastic domain switching depends on texture.

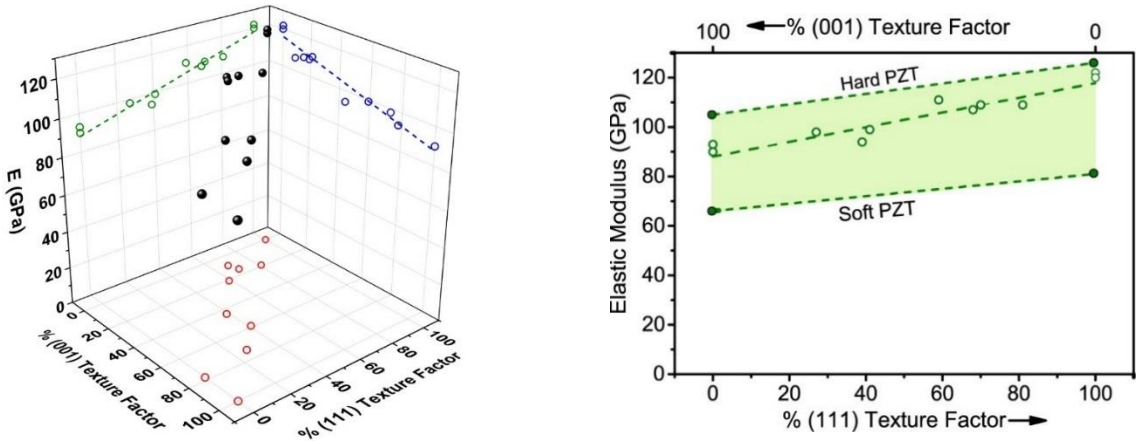

Figure 13. (a) Elastic modulus of PZT as a function of %(001) and %(111) texture factors. The scatter in the data is due to the presence of (110) texture which cannot be taken into account in the plot. **(b)** Elastic modulus as a function of %(111) texture factor: the experimental data lie within the upper and lower bounds calculated for transversely isotropic textured films by using the compliance coefficients for soft and hard bulk PZT and assuming rule of mixtures. The dashed lines correspond to the theoretically calculated moduli based on the rule of mixtures and the computed $\overline{E}_{PZT(001)}$ and $\overline{E}_{PZT(111)}$.

The open circuit modulus of PZT is plotted in Figure 13(a) demonstrating a linear relationship with %(001) and %(111) texture factors: pure (001) texture resulted in the minimum modulus value of 90±2 GPa which increased linearly with (111) texture reaching the maximum value of 122±3 GPa for pure (111) texture. The experimental moduli values were compared to theoretical predictions considering tetragonal symmetry (Appendix A). Theoretical predictions using soft and hard bulk PZT compliance coefficients yielded in-plane elastic moduli of $\overline{E}_{PZT(001)}$ = 66 GPa and $\overline{E}_{PZT(111)}$ = 81 GPa for soft PZT, and $\overline{E}_{PZT(001)}$ = 105 GPa and $\overline{E}_{PZT(111)}$ = 126 GPa

for hard PZT. These values can be considered as the lower and upper bounds for the in-plane Young's modulus corresponding to (001) and (111) PZT texture, respectively. Figure 13(b) shows the experimentally obtained Young's modulus of PZT as a function of percent (111) texture factor and the theoretical values for transversely isotropic textured films using the compliance coefficients for soft and hard bulk PZT. If the PZT composition is thought to be comprised of only (001) and (111) textures, then the rule of mixtures yields the lower and upper limits shown by dotted lines in Figure 13(b). The experimental data fit within these two bounds and lie close to the upper limit obtained for hard bulk PZT.

III.B.2. Piezoelectric Properties as a Function of Texture

Standard methods for the evaluation of the transverse piezoelectric coefficient of PZT thin films have not been established yet. The two commonly used techniques are based on **(a)** measurement of the out-of-plane displacement of unimorph microscale PZT cantilevers in response to an applied electric field and **(b)** measurement of the charge generated by laterally deformed PZT films deposited on a Si wafer [43,48,76]. The former is the most practical of the two techniques to obtain the effective transverse piezoelectric properties of freestanding thin PZT films. Unlike bulk PZT ceramics, thin PZT films are used in the form of multilayer stacks where the supporting layers and the electrodes impose significant constraints on the PZT film; therefore we often quantify the *effective piezoelectric coefficients* instead of the *true piezoelectric coefficients* of the PZT material.

The freestanding cantilevers comprised of PZT film stacks had an initial curvature due to the residual stresses developed during deposition at the different interfaces in the stacks. The transverse piezoelectric coefficients, $d_{31,f}$, were computed for various textures using the open circuit PZT moduli[1], with the aid of the PZT unimorph displacements measured with an LDV, Figure 14(a) after applying an analytical model similar to that by Weinberg [60] for a curved beam (Appendix D). Figure 14(b) shows that $d_{31,f}$ has the largest value of ~117 pm/V for pure (001) texture, which then decreases linearly as the content of (111) texture increases reaching the smallest value of ~35 pm/V for pure (111) texture. The effective piezoelectric stress coefficients for textured PZT films, $e_{31,f}$, were calculated from the strain coefficients, $d_{31,f}$, (Appendix D) and are plotted in Figure 14(c). $e_{31,f}$ generally increases with increasing %(001) texture factor and the values obtained in this study follow closely those obtained by Ledermann *et al*. [40] for the two extreme textures.

[1] The open circuit modulus of PZT does not differ significantly from its short circuit modulus due to the small piezoelectric coupling coefficient (k^2~0.12).

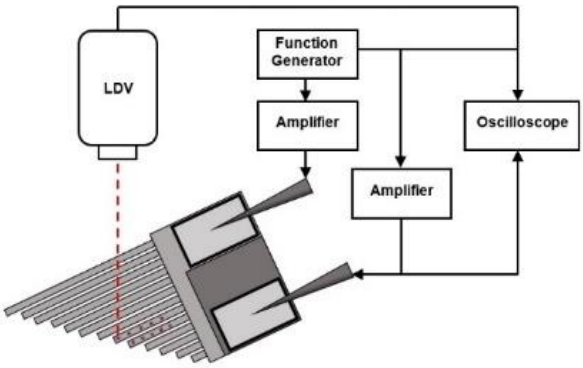

(a)

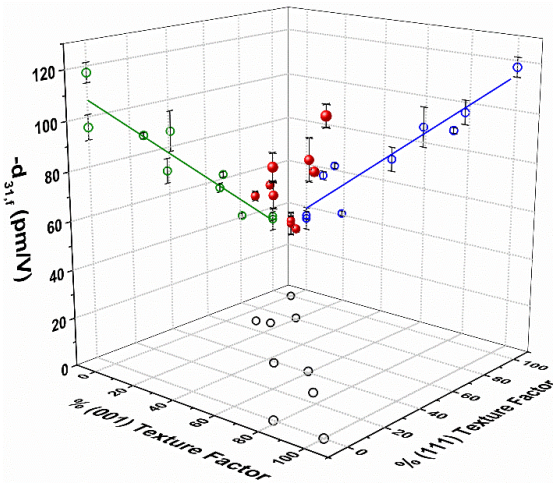

(b)

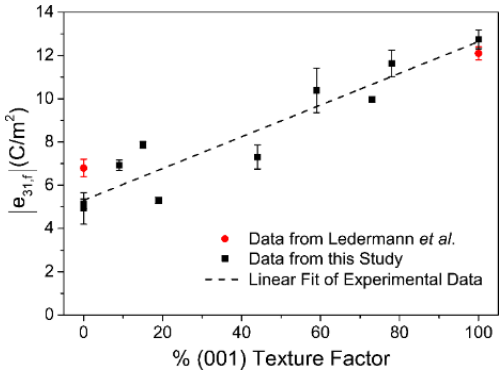

(c)

Figure 14. (a) Arrangement for the measurement of out-of-plane displacement along a cantilever beam with a laser-Doppler vibrometer (LDV). **(b)** Transverse strain coefficient, $d_{31,f}$, as a function of %(001) and %(111) texture factors computed from out-of-plane displacement data along each cantilever beam shown in Figure 1(c), which were obtained with the aid of a LDV. **(C)** Effective piezoelectric stress coefficients, $e_{31,f}$, calculated from the strain coefficients, $d_{31,f}$, as a function of %(001) texture factor.

Notably, $e_{31,f}$ varies quite linearly with %(001) texture factor. It should be emphasized that this research provided intermediate data for various percentages of (001) texture as opposed to prior literature that quantified only the extreme cases of 0% and 100% (001) texture [40]. Additionally, tip displacements of cantilevers of 50 µm length were measured using a LDV while bipolar triangular wave signals of ±10 V at a frequency of 2 Hz were applied. The results for three different textures are shown in Figure 15(a). Polarization reversals took place while applying bipolar bias. The tip displacement curves formed relatively regular butterfly loops and films with (001) preferred orientation showed significantly larger piezoelectric response than films with (111) preferred orientation for the same bias level and the same film thickness.

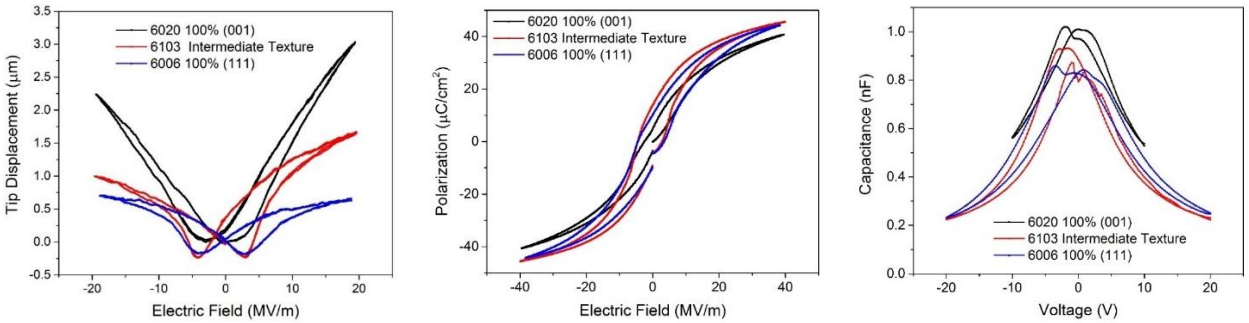

(a) **(b)** **(c)**

Figure 15. (a) Cantilever tip deflection as a function of applied electric field during bipolar biasing showing regular butterfly loops for three different PZT film textures. Note that the film with (001) texture shows much larger deflection than that with (111) texture. **(b)** P-E hysteresis loops for three different textures, **(c)** C-V sweeps for three different textures. The maximum capacitance is shown to increase with increasing (001) texture.

PE hysteresis loops, Figure 15(b) exhibited tilting, shifting, and pinching. Measurements were carried out between -20V and +20V at 50 Hz. The hysteresis loops for predominantly (001) textures and higher Pb-excess in both the $PbTiO_3$ and PZT solutions were narrower. In general, the values of maximum polarization, saturation polarization and remnant polarization decreased with increasing percentage of excess Pb in the $PbTiO_3$ layer. Capacitance vs. voltage sweeps were also performed between -20V and +20V at 10 kHz, Figure 15(c). The maximum capacitance increased with %(001) texture or with increased in excess Pb in the $PbTiO_3$ seed layer.

III.B.3. Summary of Results from Studies with Highly Textured PZT Films

The effect of texture on the open-circuit mechanical response and piezoelectric properties of 500-nm thick freestanding PZT films was investigated. The open circuit modulus varied linearly with %(001) and %(111) texture factors ranging between 90±2 GPa for pure (001) texture and 122±3 GPa for pure (111) texture. Pure (001) texture resulted in the most pronounced non-linear stress vs. strain response and (111) texture in the least non-linear response, indicating easier 90˚ domain switching for pure (001) texture, which was also corroborated by a micromechanics model. This implies that ferroelasticity, an extrinsic property of ferroelectrics, can be controlled through film texture. The piezoelectric properties were also found to depend very strongly on PZT film texture and the transverse strain and stress coefficients varied linearly with %(001) and %(111) texture factors: PZT films with higher %(001) texture content demonstrated much more pronounced piezoelectric response than those with high %(111) texture content, therefore, (001) is an optimal texture for low voltage PZT-based MEMS devices.

Appendix A: Calculation of Theoretical Elastic Moduli of Pt, TiO_2 and Tetragonal PZT

Pt has FCC crystal structure and the Pt films studied in this research had columnar grains with {111}-fiber texture. The TiO_2 films had (100) or (010) texture and body-centered tetragonal rutile crystal structure. The elastic moduli of single crystal cubic and tetragonal systems along a crystallographic $\langle hkl \rangle$ direction [77] are given by:

$$E_{\langle hkl\rangle\, cubic} = \frac{1}{s_{11} - 2\left(s_{11} - s_{12} - \frac{s_{44}}{2}\right)(\alpha^2\beta^2 + \beta^2\gamma^2 + \gamma^2\alpha^2)} \tag{A.1a}$$

$$E_{\langle hkl\rangle\, tetragonal} = \frac{1}{(\alpha^4 + \beta^4)s_{11} + \gamma^4 s_{33} + \alpha^2\beta^2(2s_{12} + s_{66}) + \gamma^2(1-\gamma^2)(2s_{13} + s_{44})} \tag{A.1b}$$

where α, β and γ are the direction cosines and s_{ij} are the compliance coefficients. The compliance coefficients, s_{ij} for single crystal Pt are s_{11}= 9.12 TPa^{-1}, s_{12}= -3.98 TPa^{-1}, s_{44}= 13.78 TPa^{-1} at 300 K [78], and for single crystal rutile are s_{11}=6.82 TPa^{-1}, s_{12}=-4.06 TPa^{-1}, s_{13}=-1.10 TPa^{-1}, s_{33}=3.24 TPa^{-1}, s_{44}=10.41 TPa^{-1}, s_{66}=5.28 TPa^{-1} [79]. By invoking transverse isotropy, Equations A.1(a,b) are averaged for an aggregate of columnar grains to obtain an estimate for the effective in-plane modulus of {111}-textured Pt and (100)-textured TiO_2:

$$\overline{E}_{Pt} = \frac{1}{2\pi}\int_{-\pi}^{\pi} \frac{d\theta}{\left(s_{11} - 2\left(s_{11} - s_{12} - 0.5s_{44}\right)\left(0.25\right)\right)} = 166 \text{ GPa} \tag{A.2a}$$

$$\overline{E}_{TiO_2} = \frac{1}{2\pi}\int_{-\pi}^{\pi} \frac{d\theta}{\left(\cos^4\left(\theta\right)s_{11} + \sin^4\left(\theta\right)s_{33} + \sin^2\left(\theta\right)\cos^2\left(\theta\right)\left(2s_{13} + s_{44}\right)\right)} = 224 \text{ GPa} \tag{A.2b}$$

For {111} Pt, the term $(\alpha^2\beta^2 + \beta^2\gamma^2 + \gamma^2\alpha^2)$ becomes 0.25 without any angular dependence, and as a result, the Pt films exhibit in-plane isotropy even at the scale of individual columnar grains. Substituting s_{ij} to Eqns. (A.2a) and (A.2b) yields the in-plane elastic modulus $\overline{E}_{Pt}$=166 GPa for {111}-texture and $\overline{E}_{TiO_2}$ = 224 GPa for (100)-texture.

The elastic modulus of polycrystalline textured PZT films can also be theoretically predicted by considering the tetragonal symmetry. The PZT films at hand had columnar grains with textures ranging from pure (001) to pure (111) fiber texture. The elastic modulus of single crystal tetragonal (*P4mm*) systems along a crystallographic <*hkl*> direction is given by Equation (A.1b).

The compliance coefficients, s_{ij}^{D}, for soft (s_{11}^{D}=15.08 TPa^{-1}, s_{12}^{D}=-9.25 TPa^{-1}, s_{13}^{D}=-3.03 TPa^{-1}, s_{33}^{D}=9.65 TPa^{-1}, s_{44}^{D}=26.46 TPa^{-1}, s_{66}^{D}=48.78 TPa^{-1}) and hard (s_{11}^{D}=9.52 TPa^{-1}, s_{12}^{D}=-4.48 TPa^{-1}, s_{13}^{D}=-1.99 TPa^{-1}, s_{33}^{D}=7.63 TPa^{-1}, s_{44}^{D}=16.05 TPa^{-1}, s_{66}^{D}=28.01 TPa^{-1}) bulk PZT ceramics at constant electric field were obtained from [50]. By invoking transverse isotropy, Equation (A.1b) was averaged for an aggregate of columnar grains to obtain an estimate for the effective in-plane modulus of (111) and (001) fiber textured PZT according to

$$\overline{E}_{PZT(001)} = \frac{1}{2\pi}\int_{-\pi}^{\pi} \frac{d\theta}{\left(\left(\sin^4(\theta)+\cos^4(\theta)\right)s_{11}+\sin^2(\theta)\cos^2(\theta)\left(2s_{12}+s_{66}\right)\right)} \tag{A.3a}$$

$$\overline{E}_{PZT(111)} = \frac{1}{2\pi}\int_{-\pi}^{\pi} \frac{d\theta}{\left(\left(\alpha^4+\beta^4\right)s_{11}+\gamma^4 s_{33}+\alpha^2\beta^2\left(2s_{12}+s_{66}\right)+\gamma^2\left(1-\gamma^2\right)\left(2s_{13}+s_{44}\right)\right)} \tag{A.3b}$$

where $\alpha \approx (0.71\cos\theta - 0.41\sin\theta)$, $\beta \approx (-0.71\cos\theta - 0.41\sin\theta)$, and $\gamma \approx 0.81\sin\theta$ for a tetragonal unit cell with *c/a*-ratio of 1.023 [80] at the morphotropic composition. Numerical evaluation of the integrals in Equations (A.3a) and (A.3b) yields in-plane elastic moduli of $\overline{E}_{PZT(001)}$ = 66 GPa and $\overline{E}_{PZT(111)}$ = 81 GPa for soft PZT, and $\overline{E}_{PZT(001)}$ = 105 GPa and $\overline{E}_{PZT(111)}$ = 126 GPa for hard PZT.

Appendix B: Modified Thompson Model for Initiation of Plastic Deformation

The derivation of the critical resolved shear stress according to modified Thompson's model is briefly reviewed here. An idealized right circular cylindrical grain with in-plane grain size d and height h, Figure B.1, is subjected to tensile stress. A dislocation loop is emitted from the film/substrate interface and expands on a {111}-type glide plane which makes an angle φ with the Pt/TiO_2 interface. The work done by the stress field once the dislocation has swept through the slip plane in this grain is approximately given by [25]:

$$W_{out} = (\tau S)b \tag{B.1}$$

where τ is the shear stress on the glide plane, b is the magnitude of the Burgers vector and S is the surface area of the glide plane given by [25]

$$S = AB(2\theta + \sin(2\theta)) \tag{B.2}$$

The lengths of the semi-major and semi-minor axes A and B, respectively, are given by

$$A = d/(2\cos\varphi), \qquad B = d/2 \tag{B.3}$$

and the angle θ is defined as

$$\theta = \cos^{-1}\left(d'/\sqrt{d^2 + h^2}\right) \tag{B.4}$$

where

$$d' = \sqrt{d^2 - \frac{h^2}{\tan^2\varphi}} \tag{B.5}$$

As the dislocation loop expands, it deposits segments of interfacial dislocations onto the Pt/TiO_2 interface, and eventually is blocked by GBs where additional segments are deposited. The side of the loop closer to the Pt/TiO_2 interface is deposited as interfacial segments until the other side expands freely and encounters the grain edges where additional segments are deposited. In such a case, the loop would look like a half-loop expanding in the metal film. The total energy of the dislocation in the final configuration is given by

$$W_{in} = LW_{side} + d'W_{bottom} \tag{B.6}$$

where L is the total length of the intercept of the glide plane with the cylindrical grain given by [25]

$$L = 4\int_0^{\theta} \sqrt{A^2\cos^2\gamma + B^2\sin^2\gamma}\; d\gamma \tag{B.7}$$

and W_{bottom} and W_{side} are the energies per unit length of the dislocation segments at the interface and at the edge of the grain.

For the geometry shown in Figure B.1, the dislocation segment at the interface is a pure screw dislocation. Following the work by Nix [11] and Freund [81] the expression for the energy per unit length of the dislocation segment at the Pt/TiO_2 interface is given by

$$W_{bottom} = W_{screw,bottom}$$
$$= \frac{b_s^2}{4\pi}\frac{2\mu_f\mu_s}{\mu_f+\mu_s}\ln\left(\beta_s\frac{h\,h_s}{b_s(h+h_s)}\right) = \frac{b^2}{4\pi}\frac{2\mu_f\mu_s}{\mu_f+\mu_s}\ln\left(\frac{h\,h_s}{b(h+h_s)}\right) \tag{B.8}$$

where $b_s = b$, since the segment is a pure screw dislocation, β_s=1 is a numerical constant taken from the work of Nix [11], h_s is the thickness of the TiO_2 underlayer, μ_s and μ_f are the shear moduli of the TiO_2 underlayer and the film, respectively.

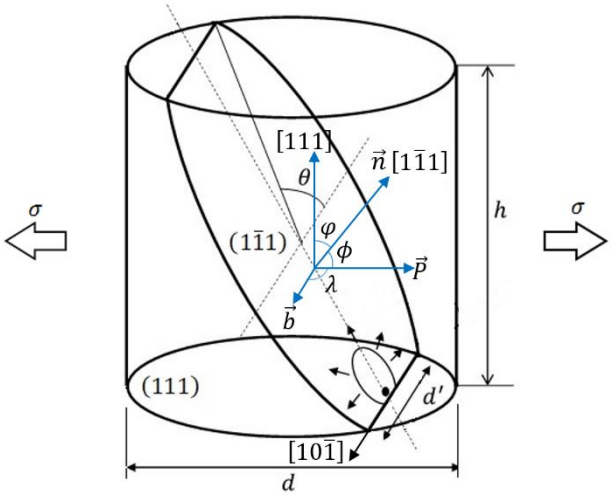

Figure B.1. Schematic of dislocation glide taking place along a {111}-slip plane which forms a truncated ellipse when it intersects a cylindrical columnar grain. The loading direction is depicted as $\vec{P}$ and makes angles ϕ and λ with the slip plane normal, $\vec{n}$ and the slip direction (Burgers vector), $\vec{b}$, respectively. The Burgers vector has been assumed to be parallel to $[10\bar{1}]$ direction because this leads to the maximum resolved shear stress on the $(1\bar{1}1)$ plane as discussed later.

The expression for the exact energy per unit length of elliptical dislocation segments in a finite domain, as for example the segments at the edges of the grain, is complex and difficult to compute. The energy depends not only on the self-energy of the segment which is modified in the presence of image forces exerted by nearby free surfaces, but also on the interaction energy of the segment with other stress fields. Due to the complexity of the problem, it suffices to consider only the self-energy per unit length of elliptical segments in an infinite elastic medium. The analytical expression for the self-energy per unit length of an elliptically shaped loop in an elastic isotropic solid is given by [82]

$$W_{side} = \frac{E}{4AE(k)} = \frac{\mu_f b^2}{4\pi(1-\nu)}(1-\eta k)\ln\left(\frac{B}{r_o}\right) \approx \frac{b^2}{4\pi(1-\nu)}\mu_f \ln\left(\frac{d}{b}\right) \tag{B.9}$$

where E is the self-energy, $4AE(k)$ is the circumference of the ellipse with $E(k)$ being the complete elliptic integral of second kind, ν is the Poisson's ratio of Pt, η is an empirical parameter, k lies between 0 and 1 and depends on the orientation of the elliptical loop with respect to the Burgers vector, and r_o is the dislocation core radius. The self-energy per unit length can be approximated to the final expression by assuming η to be a small number and $r_o = b/2$. The final expression for the self-energy per unit length is identical to the one used in Thompson's model [12].

At the critical resolved shear stress, the work done by the stress field should be just enough for the dislocation half-loop to expand and be deposited at GBs and the Pt/TiO_2 interface. Thus, by equating Equations B.1 and B.6, we have

$$\tau_{crit} = \frac{1}{Sb}(LW_{side} + d'W_{bottom}) \tag{B.10}$$

The stress generated as a result of uniaxial tension can be resolved into a shear stress on a {111}-type glide plane if the orientations of the slip plane and the slip direction with respect to the loading direction are known. Local yielding would result when the maximum resolved shear stress reaches the critical shear stress in Equation B.10. When uniaxial tension is applied to a {111}-textured Pt film, the maximum value of the resolved shear stress to a {111} plane is

$$\tau_{max} \approx 0.47\sigma \tag{B.11}$$

where σ is the stress due to uniaxial tension, as shown in Figure B.1.

Equation B.11 can be obtained as follows. Consider that the Pt film has (111)-fiber texture and is loaded in-plane along the $\left[(1+\sqrt{3})\ \bar{2}\ (1-\sqrt{3})\right]$ direction. Slip will occur on the

$(1\bar{1}1)$ plane along the $[10\bar{1}]$ direction. The resolved shear stress is then found using the stress transformation, $\tau_{max} = \tau_{nb} = l_{ni}l_{bj}\sigma_{ij} = \sigma_{pp}l_{np}l_{bp}$ (no sum on p) $= \sigma(2/3)\left(1/\sqrt{2}\right) \approx 0.47\sigma$. The subscripts *n*, *b* and *p* are the slip plane normal, slip direction and loading direction, respectively, shown in Figure B.1, while l_{np} and l_{bp} are the cosines of the angles between the directions denoted by the pair of subscripts. Similarly, slip will occur on the $(1\bar{1}\bar{1})$, $[0\bar{1}1]$ and $(11\bar{1})$, $[1\bar{1}0]$ systems when the loading direction coincides with the directions $\left[2\ \overline{(1+\sqrt{3})}\ \left(-1+\sqrt{3}\right)\right]$ and $\left[\left(1+\sqrt{3}\right)\ \left(1-\sqrt{3}\right)\ \bar{2}\right]$ respectively. In a (111)-textured polycrystalline Pt film with the (111) plane possessing infinite rotational symmetry because of the random in-plane orientation, there are always grains for which the loading direction aligns with $\left[\left(1+\sqrt{3}\right)\ \bar{2}\ \left(1-\sqrt{3}\right)\right]$, $\left[2\ \overline{(1+\sqrt{3})}\ \left(-1+\sqrt{3}\right)\right]$ and $\left[\left(1+\sqrt{3}\right)\ \left(1-\sqrt{3}\right)\ \bar{2}\right]$ directions and they undergo local plastic deformation. Finally, the elastic limit can be obtained by equating Equation B.10 with B.11:

$$\sigma_{elastic\ limit} \approx \frac{2.12}{Sb}\left(LW_{side} + d'W_{bottom}\right) \tag{B.12}$$

The underlying assumption in Equation B.12 is that far-field uniaxial tension directly translates to the local stress around a cylindrical columnar grain. {111}-textured columnar grains exhibit in-plane isotropy, thus, the stress is approximately uniform during elastic deformation of the present films even at the microstructural level, except of course near the top and bottom surfaces. This assumption of stress uniformity holds until plastic deformation is initiated.

The expression for the length of the intercept of the glide plane with the cylindrical grain given by Equation B.7 involves an elliptic integral of second kind that is evaluated numerically. A Simpson discretization scheme, as used by Carel [25], was applied for the numerical integration.

In this analysis dislocations were assumed to emanate from the Pt/TiO_2 interface due to the presence of a dislocation network at grain-to-grain heteroepitaxial {111}Pt||(100)TiO_2 interfaces. However, the top film surface roughness could also result in stress concentrations where dislocations would nucleate. This scenario is addressed by modeling the film surface roughness as a simple sinusoidal profile, $y(x) = a_o - A_0\cos(2\pi x/\lambda)$, where A_0 and λ are the wave amplitude and wavelength, respectively, and a_o is an arbitrary constant. The maximum stress concentration factor, *SF*, corresponding to the most concave surface location, is given by $SF = 1 + 4\pi(A_0/\lambda)$ [83], decaying exponentially with depth. Setting the wave amplitude equal to the maximum valley depth recorded in AFM images and the wavelength equal to the average

grain size, the stress concentration factors for films with different thickness are plotted in Figure 4(b). The 50 nm thick films had the highest surface stress concentration factor of *SF*~2.5.

Following the analysis in [84], it is shown next that the local shear stress required for nucleation of a stable dislocation at the film free surface in the absence of thermal activation is $\tau = 2\mu_f m(2-\nu)/\left(\pi e^2(1-\nu)\right)$. For applied uniaxial tension $\sigma_{far\ field}$, the local tangential stress at the root of a surface valley is $\sigma = SF\sigma_{far\ field}$ and the maximum resolved shear stress on a {111} glide plane would be $\tau_{max} = 0.47\sigma$ according to Equation B.11. For $\tau = \tau_{max}$, $m = 0.5, e = 2.718$ and $SF = 2.5$ the minimum far field tension required for nucleation of a stable dislocation at a surface crevice is $\sigma_{far\ field} \approx 5.8\,GPa$, which is 4 times larger than the largest experimentally obtained 0.2% offset yield stress value corresponding to 100-nm thick Pt films. This result is not surprising as the surface roughness amplitude of the present films is very small compared to the surface roughness wavelength. Furthermore, experimental studies on FCC Pd nanowhiskers have reported uniaxial stress values for nucleation of surface dislocations in the range of 2-8 GPa [85]. Thus, only dislocations emanating from heteroepitaxial Pt/TiO_2 interfaces are considered in this study.

Shear stress required for nucleation of a stable dislocation at a free surface crevice

The energy of a semicircular dislocation loop of radius *R* emerging at a surface groove in a metal film is given by [84]

$$U^{semi} = \frac{\mu_f b^2 R}{8}\frac{(2-\nu)}{(1-\nu)}\ln\left(\frac{8mR}{e^2 r_o}\right) \tag{B.13}$$

where μ_f is the shear modulus, b is the Burgers vector, ν is Poisson's ratio, m is a correction factor, r_o is the dislocation core cutoff radius and e is the base of the natural logarithm. The work done by the applied load is

$$W^{stress} = \frac{1}{2}\pi R^2 \tau b \tag{B.14}$$

where τ is the local shear stress on a {111} glide plane driving the dislocation loop. The total potential energy is given by

$$E = \frac{\mu_f b^2 R}{8}\frac{(2-\nu)}{(1-\nu)}\ln\left(\frac{8mR}{e^2 r_o}\right) - \frac{1}{2}\pi R^2 \tau b \tag{B.15}$$

According to [84], dislocation emission at the root of a crevice in the absence of thermal activation will take place when

$$\frac{\partial E}{\partial R} = \frac{\mu_f b^2}{8}\frac{(2-\nu)}{(1-\nu)}\ln\left(\frac{8mR}{er_o}\right) - \pi R\tau b = 0\,;\ \frac{\partial^2 E}{\partial R^2} = \frac{\mu_f b^2}{8R}\frac{(2-\nu)}{(1-\nu)} - \pi\tau b = 0 \qquad \text{(B.16)}$$

The critical local shear stress on a glide plane, required for dislocation nucleation at a surface groove is obtained by solving Equations B.16 simultaneously and setting $r_o = b/2$, to obtain:

$$\tau = \frac{2\mu_f m}{\pi e^2}\frac{(2-\nu)}{(1-\nu)} \qquad \text{(B.17)}$$

Appendix C: Micromechanics Model for Non-linear Response of (111) and (001) PZT Films

The experimental stress vs. strain response in Figure 12 shows that (001) textured PZT exhibits the most non-linearity compared to (111) textured PZT, which exhibits the least amount of non-linearity. Such non-linearities are due to ferroelasticity; a polycrystalline ferroelectric material at the morphotropic phase boundary (MPB) of any texture shows considerable nonlinear macroscopic strain due to non-180˚ domain switching [86]. The non-linearity in the tensile stress vs. strain response of thin film PZT [53] and bulk PZT [72,73] at the MPB has been attributed by other studies to ferroelastic 90˚ domain switching in the tetragonal phase due to stress. Ferroelastic domain switching in PZT ceramics at the MPB is complicated by concurrent in-phase domain switching (90˚ inside the tetragonal and 71˚ inside the rhombohedral phases) and interphase domain switching (tetragonal to rhombohedral phase transformation and vice-versa). In order to simplify the analysis of the observed non-linear response of the two extreme textures, only tetragonal symmetry was assumed, which is consistent with other studies [87,88]. For (001) texture, tetragonal elongations parallel to (100), (010) and (001) in crystal coordinates lead to a_1, a_2 and c domains, respectively, and for (111) texture lead to d_1, d_2 and d_3 domains, respectively.

In the case of pure (001) texture, the out-of-plane c domains can undergo either c-a_1 or c-a_2 switching depending on the crystal orientation with respect to the loading axis that lies on the plane of the film. The strain associated with $(c\text{-}a_1)$ or $(c\text{-}a_2)$ domain switching in local crystal coordinates is given by [89]:

$$\varepsilon^{(c-a_1)/(d_3^- - d_1^+)} = S_o \begin{bmatrix} 1 & 0 & 0 \\ 0 & 0 & 0 \\ 0 & 0 & -1 \end{bmatrix}, \quad \varepsilon^{(c-a_2)} = S_o \begin{bmatrix} 0 & 0 & 0 \\ 0 & 1 & 0 \\ 0 & 0 & -1 \end{bmatrix} \tag{C.1}$$

where $S_o = (c/a - 1)$ is the single crystal deformation. The films have fiber texture with in-plane isotropy and thus, the individual crystallites can take all possible in-plane orientations with respect to the loading axis. Consider n and m number of grains in which the crystal axes (100) and (010), respectively, are aligned along the loading axis and undergo $(c\text{-}a_1)$ and $(c\text{-}a_2)$ domain switching. These two particular orientations are equivalent and are chosen since domain switching along these orientations leads to maximum strain in the direction of the applied stress and thus provide the maximum energy released to decrease the total energy of the system, thus making these domain switches thermodynamically favorable, as shown in inset (i) of Figure 12(c). Considering a spherical region as an isotropic Eshelby inclusion [74,75] which provides a good description for the boundary conditions of the PZT film in a PZT stack, the total change in system's free energy per unit volume due to domain switching is:

$$\Delta U = \Delta U_{Elastic} - \Delta U_M^{\infty} + f_{90} W_{90} \tag{C.2}$$

where $\Delta U_{\text{Elastic}}$, $\Delta U_{\text{M}}^{\infty}$, f_{90} and W_{90} denote the elastic mismatch energy, the work done by the far field applied stress, the fraction of 90˚ domain switched and the energy barrier for 90˚ domain switching. The elastic mismatch energy can be estimated via Eshelby's inclusion model, and the Equation C.2 can then be written as:

$$\Delta U = \frac{E_{(001)}(7-5\nu)}{15(1-\nu^2)}\left(\sum_{n=1}^{n} f_{3-1}^{n} + \sum_{m=1}^{m} f_{3-2}^{m}\right)^2 S_o^2 - \left(\sigma\left(\sum_{n=1}^{n} f_{3-1}^{n} + \sum_{m=1}^{m} f_{3-2}^{m}\right)S_o\right) + \left(\sum_{n=1}^{n} f_{3-1}^{n} + \sum_{m=1}^{m} f_{3-2}^{m}\right) W_{90_{(001)}} \tag{C.3}$$

where $E_{(001)}$, ν, f_{3-1}^{n}, f_{3-2}^{m}, and σ are the elastic modulus for (001) texture, the Poisson's ratio, the fraction of *(c-a_1)* domains that has switched in n^{th} grain, the fraction of *(c-a_2)* domain that has switched in m^{th} grain, and the applied in-plane stress, respectively.

The total strain in (001) texture due to domain switching is computed by minimization of energy of Equation C.3:

$$\varepsilon_{DS_{(001)}} = \left(\sum_{n=1}^{n} f_{3-1}^{n} + \sum_{m=1}^{m} f_{3-2}^{m}\right) S_o = \frac{15(1-\nu^2)}{2E_{(001)}(7-5\nu)}\left(\sigma - \frac{W_{90_{(001)}}}{S_o}\right) \tag{C.4}$$

Interestingly, if the orientation of maximum strain due to domain switching coincides with the direction of applied stress, the total fraction of domain switching remains the same even if we consider the inclusion as a single grain undergoing only one type of switching.

In the case of pure (111) texture in the tetragonal phase, combinations of d_1, d_2 and d_3 domains, taken two at a time, form normal twin domain boundaries. In order to maintain charge neutrality of the interface, the polarization of adjacent domains must alternate. For example, twin domain patterns, such as d_3^-/d_1^+, d_3^+/d_2^- and d_2^+/d_1^-, have been theoretically predicted as well as experimentally observed in tetragonal PZT [90,91]. When an in-plane stress is applied, 90˚ domain switching may occur when one of *d* domain switches to the other across a twin boundary. Such 90˚ domain switching in the tetragonal phase in (111) textured PZT films has been experimentally observed with applied electric field [91,92]. Considering (100), (010) and (001) as the coordinate axes, a 90˚ domain switch from a d_3^- to a d_1^+ domain generates the strain given by Equation C.1. This strain must be resolved on the (111) plane and the maximum in-

plane (ε'_{11}) component can be found by transformation of strain. For example, this strain tensor in the [-(1+√3) 2 (-1+√3)], [(1-√3) -2 (1+√3)], [111] coordinate system is:

$$\varepsilon'^{(d_3^- - d_1^+)} = S_o \begin{bmatrix} 0.5774 & 0 & -0.5774 \\ 0 & -0.5774 & -0.5774 \\ -0.5774 & -0.5774 & 0 \end{bmatrix} \tag{C.5}$$

As noted before, the analysis of 90˚ domain switching in a single grain with d_3^-/d_1^+ domains will provide the total volume fraction of domains subjected to 90˚ domain switching in the (111) texture. A uniaxial stress σ is applied along the [-(1+√3) 2 (-1+√3)] direction as shown in inset (ii) of Figure 12(c). Considering a spherical grain as an isotropic Eshelby inclusion, the total change in the system's free energy per unit volume due to $(d_3^- - d_1^+)$ domain switching in a single grain is given by:

$$\Delta U = \frac{E_{(111)}(7-5\nu)}{15(1-\nu^2)}\left(f_{90_{(111)}} S_o\right)^2 - 0.5774\left(\sigma f_{90_{(111)}} S_o\right) + f_{90_{(111)}} W_{90_{(111)}} \tag{C.6}$$

where $E_{(111)}$ is the elastic modulus for (111) texture.

The total strain due to domain switching for (111) texture can be calculated by minimization of energy of Equation C.6:

$$\varepsilon_{DS_{(111)}} = \frac{15(1-\nu^2)}{2E_{(111)}(7-5\nu)}(0.5774^2)\left(\sigma - \frac{W_{90_{(111)}}}{0.5774 S_o}\right) \tag{C.7}$$

Under uniaxial tension, the total strain at a particular stress is given by the sum of the elastic strain and the strain due to 90˚ domain switching as:

$$\varepsilon_{total_{(001)}} = \frac{\sigma}{E_{(001)}} + \frac{15(1-\nu^2)}{2E_{(001)}(7-5\nu)}\left(\sigma - \sigma_{th_{(001)}}\right) \tag{C.8a}$$

$$\varepsilon_{total_{(111)}} = \frac{\sigma}{E_{(111)}} + \frac{15(1-\nu^2)}{2E_{(111)}(7-5\nu)}(0.5774^2)\left(\sigma - \sigma_{th_{(111)}}\right) \tag{C.8b}$$

where $\sigma_{th_{(001)}} = W_{90_{(001)}}/S_o$ and $\sigma_{th_{(111)}} = W_{90_{(111)}}/(0.5774 S_o)$ are fitting parameters. There is no strain due to domain switching below σ_{th}, which is the threshold stress for 90˚ domain switching. Figure 12(c) shows that Equations C.8(a,b) can predict reasonably well the

experimental stress vs. strain response with the same values for the fitting parameter $\sigma_{th_{(001)}} = \sigma_{th_{(111)}} = 220$ MPa and $\nu = 0.3$. The model provides the total fraction of 90˚ domain switching as 10% and 17% for (111) and (001) textures, respectively, and suggests that the extrinsic property of ferroelastic domain switching depends on texture.

Appendix D: Calculation of Transverse Piezoelectric Coefficients

Modifying Weinberg's model [60] for a curved multilayer composite beam with initial radius of curvature R_0 that is much larger than the dimensions of the beam cross-section, results in the following relation between the radius of curvature, R and the applied electric field, $\boldsymbol{E_{PZT}}$:

$$\frac{1}{R} = \frac{1}{R_0} - \frac{d_{31}(z_{PZT} Y_{PZT} A_{PZT} \mathbf{E}_{PZT})}{\sum_i Y_i (I_i + A_i z_i^2)} \tag{D.1}$$

where z_i, Y_i, I_i, and A_i represent for layer i the distance from neutral axis, the Young's modulus, the moment of inertia, and the cross-sectional area, respectively. The cantilever beams comprised of SiO_2-TiO_2-Pt-PZT-Pt stacks had a small segment near the fixed end resembling "webbed feet", as shown in Figure D.1(a). A thin layer (~300 nm) of SiO_2 connected the individual cantilever beams in the array, making difficult the application of a simple analysis. To this effect, each beam is considered as the combination of two segments, as shown in Figure D.1(b). The initial radius of curvature is assumed to be the same for both segments 1 and 2 as shown in the example beam profile measured with a confocal microscope in Figure D.1(c).

Equation D.1 then relates the radius of curvature of segment 1, R_1 and segment 2, R_2 with the applied electric field. It can be shown that when an electric field $\boldsymbol{E_{PZT}}$ is applied, the following relation holds for all textured PZT films:

$$0.98 \leq \frac{\left(\frac{1}{R_2} - \frac{1}{R_0}\right)}{\left(\frac{1}{R_1} - \frac{1}{R_0}\right)} \leq 0.99 \tag{D.2}$$

Equation D.2 shows that the radius of curvature induced by the applied electric field is roughly the same in each of the two beam segments. For this reason, it has been assumed that the entire beam has the same radius of curvature along its entire length. Additional assumptions are:

$$w(0, \boldsymbol{E}) \approx 0 \tag{D.3a}$$

$$\left.\frac{\mathrm{d}w}{\mathrm{d}x}\right|_{(0,\mathbf{E})} = \left.\frac{\mathrm{d}w}{\mathrm{d}x}\right|_{(0,0)} \tag{D.3b}$$

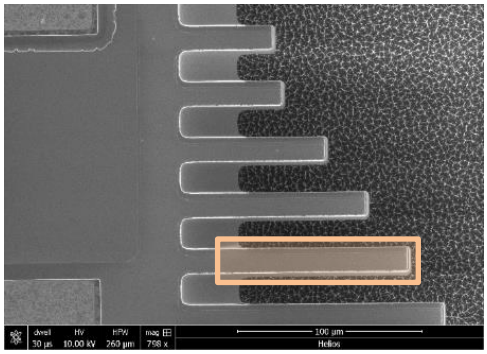

(a)

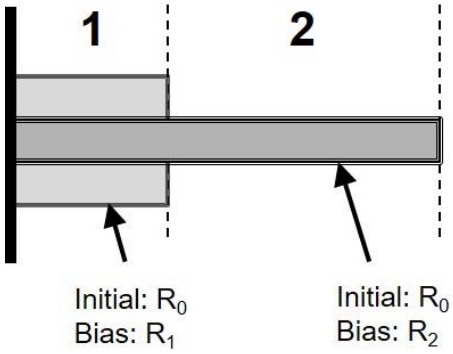

(b)

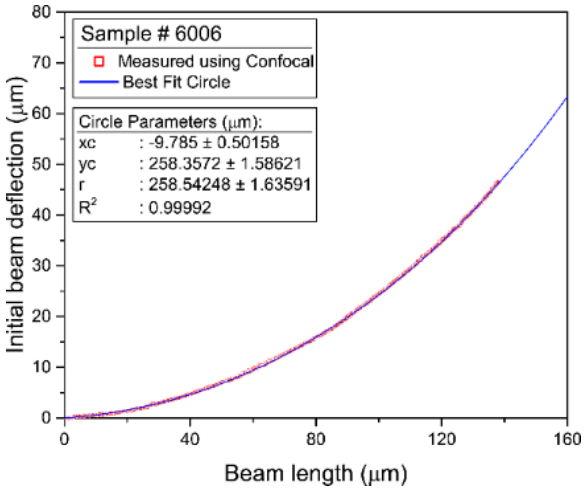

(c)

Figure D.1. (a) SEM image of cantilever beam array. The colored box points to an individual beam. **(b)** Cantilever beam comprised of two segments: Segment 1 has an additional SiO_2 layer. **(c)** Beam profile measured with a confocal microscope, showing a constant curvature in segments 1 and 2. The blue line is the best fit circle.

With these assumptions, the out-of-plane displacement $(\delta\text{-}\delta_o)$ at a distance x from the fixed end can be related to the applied electric field $\boldsymbol{E}$ as:

$$(\delta - \delta_o) = \frac{x^2}{2}\left(-\frac{d_{31}(z_{PZT}Y_{PZT}A_{PZT}\boldsymbol{E}_{PZT})}{\sum_i Y_i(I_i + A_i z_i^2)}\right) \tag{D.4}$$

Equation D.4 shows that the out-of-plane displacement is proportional to the applied electric field $\boldsymbol{E}$ and to the square of the distance from the fixed end. Figure D.2 shows the validity of the model for the textured PZT films since experimental data demonstrated a similar dependence.

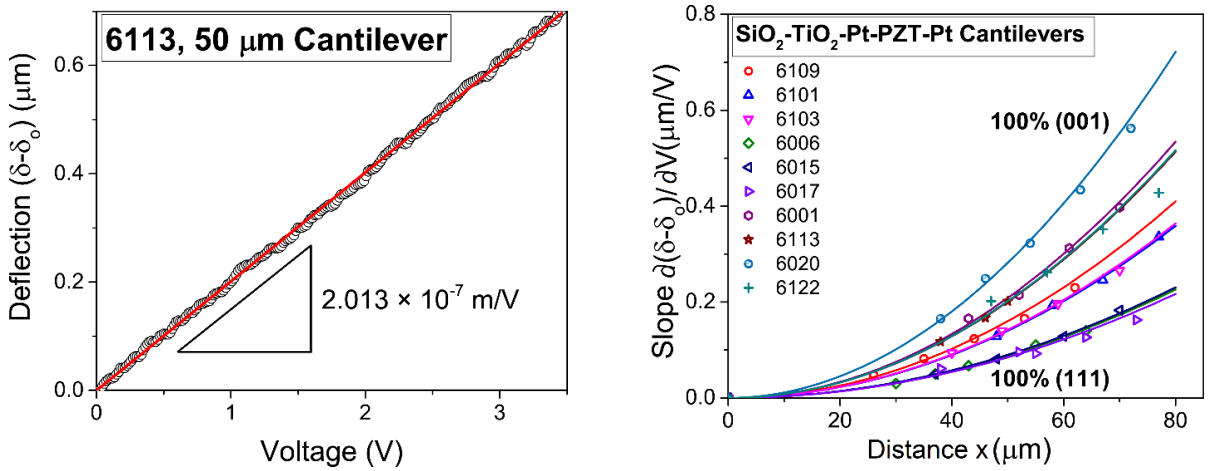

(a) **(b)**

Figure D.2 (a) Out-of-plane displacement as a function of applied voltage. **(b)** Slope as a function of distance from the fixed end showing parabolic dependence.

The effective piezoelectric stress coefficients, $e_{31,f}$ can be calculated for textured PZT from the strain coefficients, $d_{31,f}$, using the relation [76]

$$e_{31,f} = \frac{d_{31,f}}{s_{11}^E + s_{12}^E} \tag{D.5}$$

where s_{ij}^E are the compliance coefficients at constant electric field, i.e. under short circuit conditions. The short circuit compliance coefficients are assumed not to differ much from the open circuit compliance coefficients. Transverse isotropy provides: $s_{11}^E = 1/Y_{PZT}$ and $s_{12}^E = -\nu_{PZT}/Y_{PZT}$, where ν_{PZT} is the Poisson's ratio (assumed equal to 0.3 without orientation dependence) of textured PZT under open circuit conditions.

References

[1] M.J. Kobrinsky, C.V. Thompson, “The thickness dependence of the flow stress of capped and uncapped polycrystalline Ag thin films”, Appl. Phys. Lett. 73, pp. 2429–2431, (1998).

[2] R. Venkatraman, J.C. Bravman, “Separation of film thickness and grain boundary strengthening effects in Al thin films on Si”, J. Mater. Res. 7, pp. 2040–2048, (1992).

[3] H.D. Espinosa, B.C. Prorok, B. Peng, “Plasticity size effects in free-standing submicron polycrystalline FCC films subjected to pure tension”, J. Mech. Phys. Solids 52, pp. 667–689, (2004).

[4] R.P. Vinci, E.M. Zielinski, J.C. Bravman, “Thermal strain and stress in copper thin films, Thin Solid Films”, 262, pp. 142–153, (1995).

[5] R-M. Keller, S.P. Baker, E. Arzt, “Quantitative analysis of strengthening mechanisms in thin Cu films: Effects of film thickness, grain size, and passivation”, J. Mater. Res. 13, pp. 1307–1317, (1998).

[6] M. Hommel, O. Kraft, “Deformation behavior of thin copper films on deformable substrates”, Acta Mater. 49, pp. 3935–3947, (2001).

[7] G. Dehm, T.J. Balk, H. Edongué, E. Arzt, “Small-scale plasticity in thin Cu and Al films”, Microelectron. Eng. 70, pp. 412–424, (2003).

[8] A.A. Taylor, S.H. Oh, G. Dehm, “Microplasticity phenomena in thermomechanically strained nickel thin films”, J. Mater. Sci. 45, pp. 3874–3881, (2010).

[9] M. Murakami, “Thermal strain in thin lead films III: Dependences of the strain on film thickness and on grain size”, Thin Solid Films 59, pp. 105–116, (1979).

[10] L.B. Freund, “The stability of a dislocation threading a strained layer on a substrate”, J. Appl. Mech. 54, pp. 553–557, (1987).

[11] W.D. Nix, “Mechanical properties of thin films”, Metall. Trans. A, 20 (1989) 2217–2245.

[12] C.V. Thompson, “The yield stress of polycrystalline thin films”, J. Mater. Res. 8, pp. 237–238, (1993).

[13] G. Dehm, T. Wagner, T.J. Balk, E. Arzt, “Plasticity and Interfacial Dislocation Mechanisms in Epitaxial and Polycrystalline Al Films Constrained by Substrates”, J. Mater. Sci. Technol. 18, pp. 113–117, (2002).

[14] G. Dehm, E. Arzt, “In situ transmission electron microscopy study of dislocations in a polycrystalline Cu thin film constrained by a substrate”, Appl. Phys. Lett. 77, pp. 1126–1128, (2000).

[15] B. von Blanckenhagen, P. Gumbsch, E. Arzt, “Dislocation sources and the flow stress of polycrystalline thin metal films”, Philos. Mag. Lett. 83, pp. 1–8, (2003).

[16] P. Majumder, R. Katamreddy, C.G. Takoudis, “Characterization of atomic layer deposited ultrathin HfO_2 film as a diffusion barrier in Cu metallization”, MRS Proc. 990, pp. 97–102, (2007).

[17] J.S. Reid, E. Kolawa, C.M. Garland, M.-A. Nicolet, F. Cardone, D. Gupta, R.P. Ruiz, “Amorphous (Mo, Ta, or W)–Si–N diffusion barriers for Al metallizations”, J. Appl. Phys. 79, pp. 1109-1115, (1996).

[18] G.R. Fox, R.G. Polcawich, D.M. Potrepka, “Thermally oxidized seed layers for the production of {001} textured electrodes and PZT devices and method of making”, US 8866367 B2, (2014).

[19] D.M. Potrepka, G.R. Fox, L.M. Sanchez, R.G. Polcawich, “Pt/TiO_2 growth templates for enhanced PZT films and MEMS devices”, MRS Proc. 1299, pp. 67–72, (2011).

[20] L.M. Sanchez, D.M. Potrepka, G.R. Fox, I. Takeuchi, R.G. Polcawich, “Improving PZT Thin Film Texture Through Pt Metallization and Seed Layers”, MRS Proc. 1299, pp. 53–58, (2011).
[21] X-H. Du, J. Zheng, U. Belegundu, K. Uchino, “Crystal orientation dependence of piezoelectric properties of lead zirconate titanate near the morphotropic phase boundary”, Appl. Phys. Lett. 72, pp. 2421-2423, (1998).
[22] K.N. Jonnalagadda, I. Chasiotis, S. Yagnamurthy, J. Lambros, J. Pulskamp, R. Polcawich, M. Dubey, “Experimental investigation of strain rate dependence of nanocrystalline Pt films”, Exp. Mech. 50, pp. 25–35, (2010).
[23] J.M. Gere, B.J. Goodno, “Mechanics of Materials”, Seventh Edition, Cengage Learning, (2009).
[24] R. Hill, “The elastic behaviour of a crystalline aggregate”, Proc. Phys. Soc. A 65, p. 349, (1952).
[25] R. Carel, “Grain Growth and Texture Evolution in Thin Films”, PhD Thesis, MIT (1995).
[26] W.F. Hosford, “Mechanical Behavior of Materials”, Cambridge University Press, (2005).
[27] M.F. Ashby, “The deformation of plastically non-homogeneous materials”, Philos. Mag. 21, pp. 399–424, (1970).
[28] K.T. Ramesh, “Nanomaterials”, Springer US, Boston, MA, (2009).
[29] W.O. Soboyejo, T.S. Srivatsan, “Advanced Structural Materials”, CRC Press, (2006).
[30] N. Hansen, “Boundary strengthening in undeformed and deformed polycrystals”, Mater. Sci. Eng. A 409, pp. 39–45, (2005).
[31] S. Hyun, O. Kraft, R.P. Vinci, “Mechanical behavior of Pt and Pt–Ru solid solution alloy thin films”, Acta Mater. 52, pp. 4199–4211, (2004).
[32] T.J. Rupert, “Strain localization in a nanocrystalline metal: Atomic mechanisms and the effect of testing conditions”, J. Appl. Phys. 114, p. 033527, (2013).
[33] M. Chen, E. Ma, K.J. Hemker, H. Sheng, Y. Wang, X. Cheng, “Deformation twinning in nanocrystalline aluminum”, Science 300, pp. 1275–1277, (2003).
[34] S.H. Oh, M. Legros, D. Kiener, P. Gruber, G. Dehm, “In situ TEM straining of single crystal Au films on polyimide: Change of deformation mechanisms at the nanoscale”, Acta Mater. 55, pp. 5558–5571, (2007).
[35] P.A. Gruber, E. Arzt, R. Spolenak, “Brittle-to-ductile transition in ultrathin Ta/Cu film systems”, J. Mater. Res. 24, pp. 1906–1918, (2011).
[36] M. Murata, T. Kondoh, T. Yagi, N. Funatsu, K. Tanaka, H. Tsukuni, K. Ohno, “High-Resolution Piezo Inkjet Printhead Fabricated by Three Dimensional Electrical Connection Method using through Glass VIA”, 2009 IEEE 22nd International Conference on Micro Electro Mechanical Systems, IEEE, pp. 507–510, (2009).
[37] G.L. Smith, J.S. Pulskamp, L.M. Sanchez, D.M. Potrepka, R. M. Proie, T. G. Ivanov, R.Q. Rudy, "PZT-based piezoelectric MEMS technology." J. Am. Ceram. Soc. 95, pp. 1777-1792, (2012).
[38] P. Muralt, “Piezoelectric Films for Innovations in the Field of MEMS and Biosensors”, Piezoelectricity, Vol. 114, Springer Berlin Heidelberg, Berlin, Heidelberg, pp. 351–376, (2008).
[39] J.R. Bronson, J.S. Pulskamp, R.G. Polcawich, C.M. Kroninger and E.D. Wetzel, “PZT MEMS Actuated Flapping Wings for Insect-Inspired Robotics”, 2009 IEEE 22nd International Conference on Micro Electro Mechanical Systems, IEEE, pp. 1047–1050, (2009).

[40] N. Ledermann, P. Muralt, J. Baborowski, S. Gentil, K. Mukati, M. Cantoni, A. Seifert, and N. Setter, "{1 0 0}-Textured, piezoelectric $Pb(Zr_x, Ti_{1-x})O_3$ thin films for MEMS: integration, deposition and properties", Sensors Actuators A Phys. 105, pp. 162-170, (2003).

[41] X. Du, J. Zheng, U. Belegundu, and K. Uchino, "Crystal orientation dependence of piezoelectric properties of lead zirconate titanate near the morphotropic phase boundary", Appl. Phys. Lett. 72, pp. 2421-2423, (1998).

[42] S. Trolier-McKinstry and P. Muralt, "Thin Film Piezoelectrics for MEMS", J. Electroceramics 12, pp. 7-17, (2004).

[43] I. Kanno, H. Kotera, and K. Wasa, "Measurement of transverse piezoelectric properties of PZT thin films", Sensors Actuators A Phys. 107, pp. 68-74, (2003).

[44] L.M. Sanchez, D.M. Potrepka, G.R. Fox, I. Takeuchi, K. Wang, L. A. Bendersky, and R.G. Polcawich, "Optimization of PbTiO3 seed layers and Pt metallization for PZT-based piezoMEMS actuators", J. Mater. Res. 28, pp. 1920-1931, (2013).

[45] S. Mhin, K. Nittala, C. Cozzan, K. Kim, D.S. Robinson, L.M. Sanchez, R.G. Polcawich, and J.L. Jones, "Role of the $PbTiO_3$ Seed Layer on the Crystallization Behavior of PZT Thin Films", Journal of the American Ceramics Society 98, pp. 1407-1412, (2015).

[46] P. Muralt, T. Maeder, L. Sagalowicz, S. Hiboux, S. Scalese, D. Naumovic, R.G. Agostino, N. Xanthopoulos, H.J. Mathieu, L. Patthey, and E.L. Bullock, "Texture control of $PbTiO_3$ and $Pb(Zr,Ti)O_3$ thin films with TiO_2 seeding", J. Appl. Phys. 83, pp. 3835-3841, (1998).

[47] S. Hiboux and P. Muralt, "Mixed titania-lead oxide seed layers for PZT growth on Pt(111): a study on nucleation, texture and properties", J. Eur. Ceram. Soc. 24, pp. 1593-1596, (2004).

[48] D. Ambika, V. Kumar, K. Tomioka, and I. Kanno, "Deposition of PZT thin films with (001), (110), and (111) crystallographic orientations and their transverse piezoelectric characteristics", Adv. Mater. Lett. 3, pp. 102-106, (2012).

[49] Q.-M. Wang, Y. Ding, Q. Chen, M. Zhao, and J. Cheng, "Crystalline orientation dependence of nanomechanical properties of $Pb(Zr_{0.52}Ti_{0.48})O_3$ thin films", Appl. Phys. Lett. 86, p. 162903, (2005).

[50] P. Delobelle, G.S. Wang, E. Fribourg-Blanc, and D. Remiens, "Indentation modulus and hardness of Pb(Zr, Ti)O3 sol–gel films deposited on Pt and LaNiO3 electrodes", J. Eur. Ceram. Soc. 27, pp. 223-230, (2007).

[51] H. Wu, L. Wu, Q. Sun, W. Fei, and S. Du, "Mechanical properties of sol–gel derived lead zirconate titanate thin films by nanoindentation", Appl. Surf. Sci. 254, pp. 5492-5496, (2008).

[52] I. Kanno, S. Fujii, T. Kamada, and R. Takayama, "Piezoelectric properties of c-axis oriented $Pb(Zr,Ti)O_3$ thin films", Appl. Phys. Lett. 70, pp. 1378-1380, (1997).

[53] S. Yagnamurthy, I. Chasiotis, J. Lambros, R.G. Polcawich, J.S. Pulskamp, and M. Dubey, "Mechanical and Ferroelectric Behavior of PZT-Based Thin Films", J. Microelectromechanical Syst. 20, pp. 1250-1258, (2011).

[54] S. Wakabayashi, H. Totani, M. Sakata, M. Ikeda, H. Goto, M. Takeuchi, and T. Yada, "Study on mechanical characteristics of PZT thin film for sensors and actuators" in *Proc. SPIE*, edited by K.W. Markus, pp. 304–314, (1995).

[55] S.-G. Hong, M. Kim, S.-B. Lee, and C. S. Lee, "Characterization of Deformation Behaviors and Elastic Moduli of Multilayered Films in Piezoelectric Inkjet Head", J. Microelectromechanical Syst. 17, pp. 1155-1163, (2008).

[56] S. Watanabe, T. Fujiu, and T. Fujii, "Effect of poling on piezoelectric properties of lead zirconate titanate thin films formed by sputtering", Appl. Phys. Lett. 66, pp. 1481-1483, (1995).

[57] D.L. Polla and L.F. Francis, “Ferroelectric thin films in micro-electromechanical systems applications”, MRS Bull. 21, pp. 59-65, (1996).
[58] J.F. Shepard, P.J. Moses, and S. Trolier-McKinstry, “The wafer flexure technique for the determination of the transverse piezoelectric coefficient (d_{31}) of PZT thin films”, Sensors Actuators A Phys. 71, pp. 133-138, (1998).
[59] D.L. DeVoe and A.P. Pisano, “Modeling and optimal design of piezoelectric cantilever microactuators”, J. Microelectromechanical Syst. 6, pp. 266-270, (1997).
[60] M.S. Weinberg, “Working equations for piezoelectric actuators and sensors”, J. Microelectromechanical Syst. 8, pp. 529-533, (1999).
[61] C. Ayela, L. Nicu, C. Soyer, E. Cattan, and C. Bergaud, “Determination of the d_{31} piezoelectric coefficient of $PbZr_xTi_{1-x}O_3$ thin films using multilayer buckled micromembranes”, J. Appl. Phys. 100, p. 054908, (2006).
[62] J. Akedo and M. Lebedev, “Piezoelectric properties and poling effect of Pb (Zr, Ti) O3 thick films prepared for microactuators by aerosol deposition”, Appl. Phys. Lett. 77, p.1710, (2000).
[63] L. Lian and N.R. Sottos, “Effects of thickness on the piezoelectric and dielectric properties of lead zirconate titanate thin films”, Journal of Applied Physics 87, pp. 3941, (2000).
[64] K. Kakimoto, H. Kakemoto, S. Fujita, and Y. Masuda, “Stoichiometry and crystal orientation of YAG-PLD derived ferroelectric PZT thin film”, Journal of the American Ceramics Society 85, pp. 1019, (2004).
[65] L. Lian and N.R. Sottos, “Stress effects in sol-gel derived ferroelectric thin films”, J. Appl. Phys. 95, pp. 629-634, (2004).
[66] T.A. Berfield, R.J. Ong, D.A. Payne, and N.R. Sottos, “Residual stress effects on piezoelectric response of sol-gel derived lead zirconate titanate thin films”, J. Appl. Phys. 101, p. 024102, (2007).
[67] L.M. Sanchez, “Optimization of PZT (52/48) through Improved Platinum Metallization, Use of a $PbTiO_3$ Seed Layer, and Fine Tuning of Annealing Conditions for Applications in Multilayer Actuator MEMS Technology”, PhD Thesis, University of Maryland, (2014).
[68] K. Budd, S.K. Key, and D.A. Payne, “Sol-gel processing of $PbTiO_3$, $PbZrO_3$, PZT and PLZT thin films”, *Br. Ceram. Proc.*, pp. 107, (1985)
[69] M. Birkholz, “Thin Film Analysis by X-Ray Scattering”, Wiley-VCH Verlag GmbH & Co. KGaA, Weinheim, FRG, (2005).
[70] D. Das, B. Power, J.P. Martin, R.G. Polcawich, and I. Chasiotis, “Role of oxide seed layer in plastic response of epitaxially grown textured metal films”, Acta Mater. 112, pp. 390-402, (2016).
[71] C.F. Herrmann, F.W. DelRio, S.M. George, and V.M. Bright, “Properties of atomic layer deposited Al_2O_3/ZnO dielectric films grown at low temperature for RF MEMS”, *Micromach. Microfabr. Process Technol. X*, edited by M.-A. Maher and H.D. Stewart, pp. 159–166, (2005).
[72] T. Tanimoto, K. Yamamoto, and T. Morii, “Nonlinear stress-strain behavior of piezoelectric ceramics under tensile loading”, in Proc. 1994 IEEE Int. Symp. Appl. Ferroelectr. (IEEE, 1994), pp. 394–397, (1994).
[73] H. Cao and A.G. Evans, “Nonlinear Deformation of Ferroelectric Ceramics”, Journal of the American Ceramics Society 76, pp. 890-896, (1993).
[74] T. Mura, “Micromechanics of Defects in Solids”, 2nd ed., Martinus Nijhof, Dordrecht, (1987).

[75] W. Yang, H.T. Wang, F. Fang, and Y.Q. Cui, “Unconventional domain band structure at the crack tip in ferroelectric ceramics”, Theor. Appl. Fract. Mech. 37, pp. 397-408, (2001).
[76] M.A. Dubois, P. Muralt. “Measurement of the effective transverse piezoelectric coefficient $e_{31,f}$ of AlN and $Pb(Zr_xTi_{1-x})O_3$ thin films”, Sensors and Actuators A: Physical 77.2, pp. 106-112, (1999).
[77] J.F. Nye, “Physical Properties of Crystals: Their Representation by Tensors and Matrices”, Oxford: At the Clarendon Press, (1957).
[78] S.M. Collard, R.B. McLellan, “High-temperature elastic constants of platinum single crystals”, Acta Metall. Mater., 40, pp. 699–702, (1992).
[79] V. Swamy, J.D. Gale, “Transferble variable-charge interatomic potential for atomistic simulation of titanium oxides”, Phys. Rev. B, 62, pp. 5406–5412, (2000).
[80] M.J. Hoffmann, M. Hammer, A. Endriss, and D.C. Lupascu, “Correlation between microstructure, strain behavior, and acoustic emission of soft PZT ceramics”, Acta Mater. 49, pp. 1301-1310 (2001).
[81] L.B. Freund, S. Suresh, “Thin Film Materials - Stress, Defect Formation and Surface Evolution”, Cambridge University Press, (2004).
[82] W.G. Wolfer, T. Okita, D.M. Barnett, “Motion and Rotation of Small Glissile Dislocation Loops in Stress Fields”, Phys. Rev. Lett., 92, p. 085507, (2004).
[83] H. Gao, “Stress concentration at slightly undulating surfaces”, J. Mech. Phys. Solids 39 pp. 443–458, (1991).
[84] G.E. Beltz, L.B. Freund, “On the Nucleation of Dislocations at a Crystal Surface”, Phys. Stat. Sol. 180, pp. 303–313, (1993).
[85] L.Y. Chen, M. He, J. Shin, G. Richter, D.S. Gianola, “Measuring surface dislocation nucleation in defect-scarce nanostructures”, Nat. Mater., 14, pp. 707–713, (2015).
[86] J.Y. Li, R.C. Rogan, E. Ustündag, and K. Bhattacharya, “Domain switching in polycrystalline ferroelectric ceramics”, Nat. Mater. 4, pp. 776-781, (2005).
[87] F. Li and D. Fang, “Simulations of domain switching in ferroelectrics by a three-dimensional finite element model”, Mech. Mater. 36, pp. 959-973, (2004).
[88] C.M. Landis, “On the Strain Saturation Conditions for Polycrystalline Ferroelastic Materials”, J. Appl. Mech. 70, pp. 470-478, (2003).
[89] F.X. Li and R.K.N.D. Rajapakse, “A constrained domain-switching model for polycrystalline ferroelectric ceramics. Part I: Model formulation and application to tetragonal materials”, Acta Mater. 55, pp. 6472-6480, (2007).
[90] A.E. Romanov, A. Vojta, W. Pompe, M.J. Lefevre, and J.S. Speck, “Domain Patterns in (111) Oriented Tetragonal Ferroelectric Films”, Phys. Status Solidi 172, pp. 225-253, (1999).
[91] R. Xu, S. Liu, I. Grinberg, J. Karthik, A.R. Damodaran, A.M. Rappe, and L.W. Martin, “Ferroelectric polarization reversal via successive ferroelastic transitions”, Nat. Mater. 14, pp. 79-86, (2015).
[92] B.J. Rodriguez, A. Gruverman, A.I. Kingon, R.J. Nemanich, and J.S. Cross, “Investigation of the mechanism of polarization switching in ferroelectric capacitors by three-dimensional piezoresponse force microscopy”, Appl. Phys. A Mater. Sci. Process. 80, pp. 99-103, (2005).